RANS-based simulation of turbulent wave boundary layer and sheet-flow sediment transport processes

David R. Fuhrman *, Signe Schløer, Johanna Sterner

Technical University of Denmark, Department of Mechanical Engineering, DK-2800 Kgs. Lyngby, Denmark

ABSTRACT

A numerical model coupling the horizontal component of the incompressible Reynolds-averaged Navier–Stokes (RANS) equations with two-equation $k-\omega$ turbulence closure is presented and used to simulate a variety of turbulent wave boundary layer processes. The hydrodynamic model is additionally coupled with bed and suspended load descriptions, the latter based on an unsteady turbulent-diffusion equation, for simulation of sheet-flow sediment transport processes. In addition to standard features common within such RANS-based approaches, the present model includes: (1) hindered settling velocities at high suspended sediment concentrations, (2) turbulence suppression due to density gradients in the water–sand mixture, (3) boundary layer streaming due to convective terms, and (4) converging–diverging effects due to a sloping bed. The present model therefore provides a framework for simultaneous inclusion of a number of local factors important within cross-shore wave boundary layer and sediment transport dynamics. The hydrodynamic model is validated for both hydraulically smooth and rough conditions, based on wave friction factor diagrams and boundary layer streaming profiles, with the results in excellent agreement with experimental and/or previous numerical work. The sediment transport model is likewise validated against oscillatory tunnel experiments involving both velocity-skewed and acceleration-skewed flows, as well as against measurements beneath real progressive waves. Model capabilities are exploited to investigate the importance of boundary layer streaming effects on sediment transport in selected velocity-skewed conditions. For the medium sand grain conditions considered, the model results suggest that streaming effects can enhance onshore sediment transport rates by as much as a factor of two. Moreover, for fine sand conditions streaming (and related convective) effects are demonstrated to potentially reverse the direction of net transport (*i.e.* from offshore to onshore) relative that predicted in oscillatory tunnel conditions. The developed model is implemented within the popular Matlab environment, and hence may be attractive for both research and educational purposes.

1. Introduction

Making accurate cross-shore sediment transport and resultant morphological predictions in the nearshore coastal environment is notoriously difficult, primarily due to the large number of local (onshore and offshore) factors that compete simultaneously. Such factors include *e.g.* turbulence (both bed-generated and breaking-induced), wave shape (both skewness and front-back asymmetry), boundary layer streaming, converging–diverging effects from a sloping bed, return currents and undertow, in addition to the effects of bed forms, just to name a few. Under storm conditions bed ripples are typically washed out, and sediments are transported within a thin layer (O(1 cm)) above the bed (*e.g.* Hassan and Ribberink, 2010). Cross-shore sediment transport processes under these so-called sheet flow conditions have been the focus of much recent

experimental and numerical work, and is likewise largely the focus of the present paper.

Models for predicting sheet-flow sediment transport beneath waves vary widely in their complexity. These range from simple quasi-steady methods (*e.g.* Nielsen and Callaghan, 2003) to very detailed two-phase approaches (*e.g.* Amoudry et al., 2008), which solve momentum equations for water and sand phases separately, including coupling forces. At an intermediate level of complexity are single-phase approaches, wherein incompressible Reynolds-averaged Navier–Stokes equations are coupled with *e.g.* one- (*e.g.* Davies and Li, 1997; Li and Davies, 2001) or two-equation (*e.g.* Holmedal and Myrhaug, 2006) turbulence closures, with suspended sediment effects typically described by an unsteady turbulent-diffusion equation. Note that a comparison of four such models having varying complexity has been conducted by Davies et al. (1997). Such methods utilize a fixed-bed approach and therefore inevitably fail to provide a detailed account *e.g.* of the inter-granular processes that occur within the mobile bed layer. Nevertheless, they have proven to be an effective and popular means of predicting net sediment transport rates for a variety of sediment

* Corresponding author. Tel.: +45 45251975; fax: +45 45884325.
  E-mail address: drf@mek.dtu.dk (D.R. Fuhrman).

and flow conditions, while maintaining reasonable computational efficiency.

Recent advances in sediment transport modeling based on two-equation turbulence closures include the work of Ruessink et al. (2009) and Hassan and Ribberink (2010), who successfully incorporated high-concentration effects (hindered settling velocities as well as turbulence damping due to density gradients in the sand–water mixture) within $k-\epsilon$ turbulence closures. The work of Guizien et al. (2003), who incorporated turbulence damping effects within a transitional $k-\omega$ turbulence closure, also merits specific mention. These models assumed uniformity in the horizontal direction, and hence did not account for boundary layer streaming effects. Holmedal and Myrhaug (2009) and Blondeaux et al. (2012), on the other hand, have recently incorporated convective-term effects within two-equation models for the study of such boundary layer streaming on sediment transport processes. These works, however, do not include the just-mentioned high-concentration effects, which can become highly important within the sheet-flow transport of fine sands, as will be demonstrated herein.

To date, no published works (to the authors' knowledge) have coupled such high concentration effects with boundary layer streaming effects within a two-equation turbulence closure approach for sediment transport simulations. This will be achieved within the present work, which will likewise demonstrate how converging–diverging bed slope effects can similarly be accounted for within such 1DV (one-dimensional vertical) methods. Hence, the present work provides something of a unified framework for coupling a number of local factors which can simultaneously contribute to cross-shore wave boundary layer and sediment transport dynamics. The added capabilities developed herein will additionally be exploited to study the quantitative, and in some instances qualitative, effects of boundary layer streaming (and related convective effects) in selected sheet-flow sediment transport conditions of interest.

The remainder of the paper is organized as follows: A description of the basic hydrodynamic and turbulence closure models is provided in Section 2, whereas description of the sediment transport model is presented in Section 3. Issues describing numerical solutions and implementation are briefly covered in Section 4. Demonstrations and validation of the model for pure hydrodynamic cases involving turbulent wave boundary layer flows are presented in Section 5. Additional comparisons with experiments involving sediment transport beneath a variety of wave shapes and sediment sizes are presented in Section 6. This section additionally covers numerical investigations involving the potential role and significance of streaming effects beneath selected conditions involving skewed waves for medium and fine sands. Conclusions are finally summarized in Section 7.

2. Hydrodynamic and turbulence model description

2.1. Governing equations

The model solves simplified versions of the horizontal component of the incompressible Reynolds-averaged Navier–Stokes (RANS) equations, combined with the two-equation $k-\omega$ turbulence closure model of Wilcox (2006) and Wilcox (2008). The considered RANS equation reads:

$$\frac{\partial u}{\partial t} = -\frac{1}{\rho}\frac{\partial p}{\partial x} + \nu \frac{\partial^2 u}{\partial y^2} + \frac{\partial}{\partial y}\left(\nu_T \frac{\partial u}{\partial y}\right) - \underline{\left(u\frac{\partial u}{\partial x} + v\frac{\partial u}{\partial y}\right)} - \frac{2}{3}\frac{\partial k}{\partial x}. \tag{1}$$

Here u and v are velocities in the (horizontal) x and (vertical) y directions, respectively, t is time, p is the pressure, ρ the water density, and ν the kinematic viscosity.

The turbulence closure model consists of two respective transport equations for the turbulent kinetic energy (per unit mass)

$$k = \frac{1}{2}\left(\overline{u'^2} + \overline{v'^2} + \overline{w'^2}\right), \tag{2}$$

where the prime superscripted variables represent turbulent velocity fluctuations, as well as the specific dissipation rate ω:

$$\frac{\partial k}{\partial t} = \nu_T\left(\frac{\partial u}{\partial y}\frac{\partial u}{\partial y}\right) - \beta^* k\omega + \frac{\partial}{\partial y}\left[\left(\nu + \sigma^*\frac{k}{\omega}\right)\frac{\partial k}{\partial y}\right] - \underline{\left(u\frac{\partial k}{\partial x} + v\frac{\partial k}{\partial y}\right)} - \underline{B} \tag{3}$$

$$\frac{\partial \omega}{\partial t} = \alpha\frac{\omega}{k}\nu_T\left(\frac{\partial u}{\partial y}\frac{\partial u}{\partial y}\right) - \beta\omega^2 + \frac{\partial}{\partial y}\left[\left(\nu + \sigma\frac{k}{\omega}\right)\frac{\partial \omega}{\partial y}\right] + \frac{\sigma_d}{\omega}\frac{\partial k}{\partial y}\frac{\partial \omega}{\partial y} - \underline{\left(u\frac{\partial \omega}{\partial x} + v\frac{\partial \omega}{\partial y}\right)} - \underline{\underline{c_{3\omega}N^2}}. \tag{4}$$

The eddy viscosity ν_T is defined by

$$\nu_T = \frac{k}{\tilde{\omega}}, \ \tilde{\omega} = \max\left\{\omega, C_{lim}\frac{|\partial u/\partial y|}{\sqrt{\beta^*}}\right\}, \tag{5}$$

where $C_{lim} = 7/8$. In Eq. (4)

$$\sigma_d = \mathcal{H}\left\{\frac{\partial k}{\partial y}\frac{\partial \omega}{\partial y}\right\}\sigma_{do}, \tag{6}$$

where $\mathcal{H}\{\cdot\}$ is the Heaviside step function, taking a value of zero when the argument is negative, and a value of unity otherwise.

In the right hand side of Eq. (3) the first term represents the *production* of turbulent kinetic energy (the rate at which kinetic energy is transferred from the mean flow to the turbulence), the second term represents *dissipation* (the rate at which turbulent kinetic energy is converted into thermal internal energy), the third term includes both molecular and turbulent *diffusion*, and the fourth and fifth (single underlined) terms includes both horizontal and vertical *convection*. The final (double underlined) term additionally incorporates *turbulence suppression* effects due to gradients in the fluid–sediment mixture. This term is not part of the standard Wilcox (2006) model, and is discussed in more detail in Section 3. The default model closure coefficients suggested by Wilcox (2006) are utilized: $\alpha = 13/25$, $\beta = \beta_0 f_\beta$, $\beta_0 = 0.0708$, $\beta^* = 9/100$, $\sigma = 1/2$, $\sigma^* = 3/5$, and $\sigma_{do} = 1/8$. Note that for two-dimensional flows, as considered herein, $f_\beta = 1$.

2.2. Second-order terms

In Eqs. (1), (3), and (4) (and Eq. (24), below) the single-underlined (convective) terms will be deemed of second-order importance, as they vanish at the limit of spatial uniformity in the x-direction. Indeed, upon non-dimensionalizing the governing RANS Eq. (1), it can be shown that these terms will scale with $a\kappa = U_{1m}/C$, relative to leading-order (i.e. non-underlined) terms for wave boundary layer flows. Note that here $a = U_{1m}T/(2\pi)$ is the characteristic amplitude of free-stream orbital motion, κ is the wave number, U_{1m} is the characteristic free-stream velocity, with T the wave period, and C the wave celerity. It can be noted that, while these convective terms are of no importance within (horizontally uniform) oscillatory tunnel flow environments, they are responsible e.g. for the important phenomenon of boundary layer streaming beneath progressive wave motions.

Assuming constant form wave propagation, all x-derivatives appearing in the second-order terms are actually replaced by time derivatives in the model via the relation

$$\frac{\partial}{\partial x} = -\frac{1}{C}\frac{\partial}{\partial t}. \tag{7}$$

This is convenient, as it allows potential effects from x-variations (*e.g.* boundary layer streaming) to be incorporated, while only requiring discretization in the vertical y-direction. Similar treatment of the horizontal gradient operator has been utilized *e.g.* by Trowbridge and Madsen (1984), Brøker (1985), Justesen (1988), Deigaard et al. (1999), and Holmedal and Myrhaug (2009).

The vertical velocity v is approximated by solving the local continuity equation

$$\frac{\partial u}{\partial x} + \frac{\partial v}{\partial y} \approx -\frac{1}{C}\frac{\partial u^{(1)}}{\partial t} + \frac{\partial v}{\partial y} = 0, \tag{8}$$

where $\partial u^{(1)}/\partial t$ is the leading-order (*i.e.* non-underlined) part of $\partial u/\partial t$ from Eq. (1). This is justifiable because all terms containing v in the governing equations are already of second-order importance, hence any errors made by this approximation will be at third-order or higher. Utilizing only the leading-order contribution of time derivatives in this fashion is convenient in the present context, as it enables evaluation of convective terms entirely within right-hand-side evaluations of the governing Eqs. (1), (3), and (4).

2.3. Turbulence suppression terms

The final double-underlined terms in Eqs. (3) and (4) describe turbulence suppression, due to density gradients in the fluid–sediment mixture. These terms are implemented analogously to recent $k-\epsilon$ modeling undertaken by Ruessink et al. (2009), where the Buoyancy flux is

$$B = \frac{\nu_T}{\sigma_p}N^2, \tag{9}$$

and the square of the so-called Brunt–Vaisala frequency N is

$$N^2 = -\frac{g}{\rho_m}\frac{\partial \rho_m}{\partial y}, \tag{10}$$

where $\rho_m = s\rho c + \rho(1-c)$ is the density of the fluid–sediment mixture, s is the relative density of the sediment, and c the suspended sediment concentration. The default closure coefficients are $\sigma_p = 0.7$, with $c_{3\omega} = 1$ for $N^2 \leq 0$ and $c_{3\omega} = 0$ for $N^2 > 0$. For reasons unknown to the authors, implementation of the full term (Eq. (10)) has been found to destabilize the k-equation (Eq. (3)). Therefore, throughout the present work the leading-order contribution to N^2 is employed:

$$N^2 = -g(s-1)\frac{\partial c}{\partial y} + O(c). \tag{11}$$

Similar treatment of this term has been utilized within the $k-\epsilon$-based sediment transport modeling of Hassan and Ribberink (2010).

Inclusion of these terms, while not standard practice, can be extremely important for flows giving rise to high suspended sediment concentrations near the bed, especially for cases involving the sheet-flow of fine sands, as will be illustrated.

2.4. Boundary conditions

The above equations are solved starting from motionless initial conditions in a single vertical dimension, subject to the following boundary conditions. A frictionless rigid lid is imposed at the top boundary, whereby vertical derivatives of u, k, and ω are set to zero. Alternatively, the bottom boundary is considered a friction wall, and a no-slip boundary condition is imposed, *i.e.* velocity variables u and v are set to zero.

At the bottom wall a zero-gradient condition is imposed for the turbulent kinetic energy density k i.e. $dk/dy = 0$, corresponding to a zero flux of turbulent kinetic energy through the sea bed. This condition is supported by experimental measurements for steady flows on rough beds (Fuhrman et al., 2010; Sumer et al., 2003). Moreover, Fuhrman et al. (2010) have demonstrated that the zero-gradient condition is more generally consistent with near-wall physics than is a more standardly utilized $k = 0$ condition, as it allows a viscous sublayer to develop naturally near smooth walls, while conveniently avoiding the creation of a fictitious viscous sublayer near rough walls. The zero-gradient condition has also been successfully utilized in (unsteady) simulations of oscillatory wave boundary flows by Fuhrman et al. (2011), involving both smooth and rough beds.

The form of the bottom boundary condition for the specific dissipation rate ω is adopted from Wilcox (2006), where

$$\omega = \frac{U_f^2}{\nu}S_R, \quad y = 0. \tag{12}$$

The factor S_R is based on the roughness Reynolds number $k_N^+ = k_N U_f/\nu$, where $k_N = 2.5d$ is Nikuradse's equivalent sand grain roughness (d being the sediment grain diameter), and $U_f = \sqrt{|\tau_b|/\rho}$ the instantaneous friction velocity, according to

$$S_R = \begin{cases} \left(\dfrac{200}{k_N^+}\right)^2, & k_N^+ \leq 5, \\ \dfrac{K_r}{k_N^+} + \left[\left(\dfrac{200}{k_N^+}\right)^2 - \dfrac{K_r}{k_N^+}\right]e^{5-k_N^+}, & k_N^+ > 5. \end{cases} \tag{13}$$

The value $K_r = 180$ is utilized herein, which has been demonstrated by Fuhrman et al. (2010) to yield standard law of the wall solutions for steady boundary layers when used in conjunction with the $\partial k/\partial y = 0$ bottom boundary condition.

2.5. Pressure gradient

A prescribed pressure gradient in Eq. (1) is used to drive the flow within the model domain. To obtain a desired free stream velocity signal u_0, this has been implemented generally as

$$\frac{1}{\rho}\frac{\partial p}{\partial x} = -\frac{\partial u_0}{\partial t} - u_0\frac{\partial u_0}{\partial x} \tag{14}$$

$$\approx \left(\frac{u_0}{\underline{C}} - 1\right)\frac{\partial u_0}{\partial t} - \underline{\underline{Su_0^2/h}} + P_x. \tag{15}$$

Here Eq. (7) has been invoked to arrive at the second-order (single underlined) term, which is only included when second-order effects are switched on. The triple-underlined term similarly accounts for convective acceleration associated with converging–diverging effects induced from a mildly-sloping bottom (see Appendix A for further explanation of this particular term), where $S = -\partial h/\partial x$ is the local bottom slope and h is the local water depth.

A constant pressure gradient P_x is also added to Eq. (15) for generality, which can be used *e.g.* to drive steady currents, within combined wave-current simulations, or to counter induced drifts generated within wave boundary layer simulations. Unless otherwise stated, $P_x = 0$ and $S = 0$ in what follows.

As discussed by many authors, variations in wave shape can be highly important in cross-shore wave boundary layer and sediment transport dynamics. Within the present model two options are included for wave boundary layer forcing. The first corresponds to a free-stream velocity having the form of a second-order Stokes signal (taking $x = 0$):

$$u_0 = U_{1m}\sin\left(\omega t'\right) - U_{2m}\cos\left(2\omega t'\right) \tag{16}$$

$$\frac{\partial u_0}{\partial t} = U_{1m}\omega\cos\left(\omega t'\right) + 2U_{2m}\omega\sin\left(2\omega t'\right) \tag{17}$$

where $t' = t + t_0$, with t_0 representing a time shift in the signal, which is determined automatically to ensure that $u_0(t = 0) = 0$ for consistency

with the motionless initial conditions. In Eqs. (16) and (17), and hereafter, the variable $\omega = 2\pi/T$ will refer to the wave angular frequency, where T is the wave period. Note that a sinusoidal free stream velocity signal is achieved e.g. by simply setting $U_{2m} = 0$, whereby $t_0 = 0$. The second signal corresponds to the more flexible wave form shape proposed recently by Abreu et al. (2010):

$$u_0 = U_w \sqrt{1 - r^2} \cdot \frac{\sin\left(\omega t'\right) + \frac{r \sin\phi}{1 + \sqrt{1 - r^2}}}{1 - r \cos\left(\omega t' + \phi\right)}, \tag{18}$$

$$\frac{\partial u_0}{\partial t} = U_w \omega \sqrt{1 - r^2} \cdot \frac{\cos\left(\omega t'\right) - r \cos\phi - \frac{r^2}{1 + \sqrt{1 - r^2}} \sin\phi \sin\left(\omega t' + \phi\right)}{\left(1 - r \cos\left(\omega t' + \phi\right)\right)^2}, \tag{19}$$

This option allows forcing velocity signals ranging from skewed (i.e. raised peaks and troughs, e.g. with $\phi = -\pi/2$ and $0 \le r \le 0.75$) to front-back asymmetric (e.g. with $\phi = 0$ and $0 \le r \le 0.75$, corresponding to "sawtooth" wave shapes more typical of the surf zone). If $r = 0$ then this shape again becomes sinusoidal, with amplitude U_w.

3. Sediment transport model description

3.1. Bed load model

The rate of bed load sediment transport q_B is calculated based on the method of Engelund and Fredsøe (1976):

$$\Phi_B = \frac{q_B}{\sqrt{(s-1)gd^3}} = 5p\left[\sqrt{\theta} - 0.7\sqrt{\theta_c}\right], \tag{20}$$

where

$$p = \left[1 + \left(\frac{\pi\mu_d}{6(\theta - \theta_c)}\right)^4\right]^{-\frac{1}{4}} \tag{21}$$

is the probability of moving grains, and the Shields parameter is defined as

$$\theta = \frac{\tau_b}{\rho g(s-1)d} = \frac{U_f^2}{(s-1)gd}. \tag{22}$$

In what follows the critical Shields parameter is set to $\theta_c = 0.045$. The coefficient of dynamic friction μ_d is here taken as a sort of calibration parameter, and is set to $\mu_d = 1.6$. This value brings the utilized bed load formula very close to that proposed recently by Wong and Parker (2006):

$$\Phi_B = 4(\theta - \theta_c)^{3/2} \tag{23}$$

for $\theta < 1$, who performed a re-analysis of the bed load relation of Meyer-Peter and Müller (1948) (i.e. with 4 conventionally replaced by 8 in Eq. (23)) using their own database. This is illustrated more clearly in Fig. 1. Note that for larger Shields parameters (roughly $\theta > 1$) typical of sheet flow conditions, Eq. (21) limits p at unity, whereby the predicted non-dimensional bed load transport Φ_B from Eq. (20) will scale as $\theta^{1/2}$ rather than $\theta^{3/2}$. This feature allows standard (3/2-power) bed load scaling at lower Shields parameters, while reducing the significance of quasi-steady bed load predictions at larger Shields parameters typical of sheet flow conditions, where unsteady effects may potentially become more important (e.g. Dohmen-Janssen et al., 2002).

3.1.1. Suspended sediment model

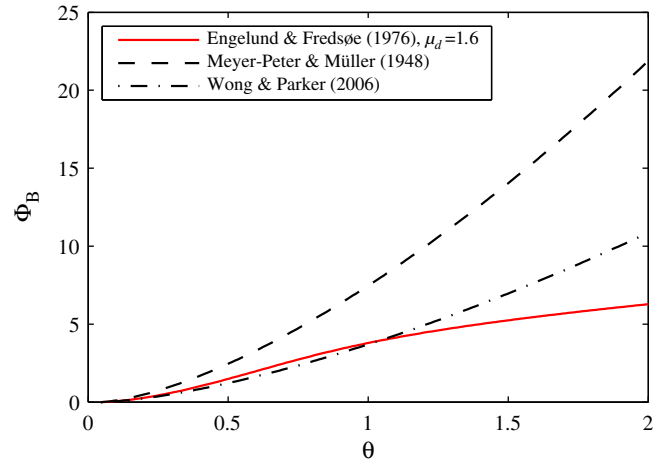The above hydrodynamic model is also coupled with a turbulent-diffusion equation for the simulation of the suspended

Fig. 1. Comparison of dimensionless bed load formulae.

sediment concentration c (see e.g. Fredsøe and Deigaard, 1992, p. 238):

$$\frac{\partial c}{\partial t} = \frac{\partial(w_s c)}{\partial y} + \frac{\partial}{\partial y}\left(\epsilon_s \frac{\partial c}{\partial y}\right) - \left(u \frac{\partial c}{\partial x} + v \frac{\partial c}{\partial y}\right), \tag{24}$$

where w_s is the settling velocity, and $\epsilon_s = \beta_s \nu_T + \nu$ is the diffusion coefficient. Following recent work (Hassan and Ribberink, 2010; Hsu and Liu, 2004; Ruessink et al., 2009) the value $\beta_s = 2$ is utilized herein (it can be noted that β_s is the inverse of the Prandtl–Schmidt number discussed in these works). Eq. (24) is solved for $b \le y \le h_m$, where $b = 2d$ is the so-called reference level, and h_m is the total height of the model domain. The instantaneous rate of suspended sediment transport is calculated via

$$q_S = \int_b^{h_m} uc\, dy. \tag{25}$$

At the lower $y = b$ boundary so-called reference concentration boundary conditions (e.g. Engelund and Fredsøe, 1976; Zyserman and Fredsøe, 1994) are imposed. While a variety of options have been implemented, throughout the present work, the classical reference concentration formula of Einstein (1950) is utilized:

$$c_b = \frac{\pi}{12}p, \tag{26}$$

where p is given by Eq. (21), again taking $\mu_d = 1.6$ for consistency. The functional dependence of c_b versus θ, as predicted by Eq. (26), is depicted in Fig. 2. As seen there, the Einstein formula tends to a constant value $c_b = 0.262$ for θ much larger than unity. This feature will in turn yield reference concentrations that are more or less the same during peaks and troughs of oscillatory sheet flows, even in cases where the free stream velocity is highly skewed (i.e. having larger magnitude peaks than troughs). This is consistent with recent laboratory experiments involving oscillatory flows over sand beds made by O'Donoghue and Wright (2004a), who found that the concentration at this level is indeed nearly constant throughout the flow cycle, even for highly skewed velocity signals. Note also that the previously mentioned constant $c_b = 0.262$ from the Einstein formula, is in excellent agreement with the constant value $c_b \approx 0.44c_{max} = 0.264$ (taking the maximum concentration as $c_{max} = 0.6$) suggested by the experiments of O'Donoghue and Wright (2004a).

Additionally, to prevent forcing $c_b = 0$ during periods of flow reversal, the actual c_b value retained during simulations is taken as the maximum of that computed from the reference concentration formula and that extrapolated from the two points nearest the bed. This prevents un-physical "overloading" conditions (i.e. where reference c_b is forced
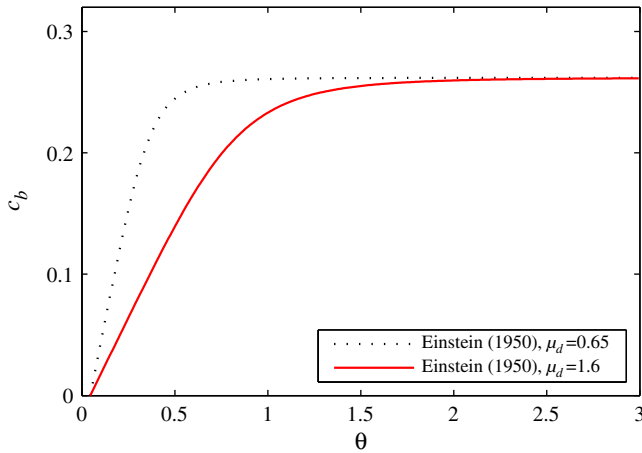
Fig. 2. A plot showing Einstein's reference concentration c_b function *versus* Shields parameter θ.

to be smaller than the concentration immediately above) from ever occurring in the model.

It is well known that at high concentrations the settling velocity becomes reduced, compared to the settling velocities of individual grains (*e.g.* Fredsøe and Deigaard, 1992). Such hindered settling effects are taken into account by allowing the settling velocity w_s to depend on the local suspended sediment concentration according to Richardson and Zaki (1954)):

$$w_s = w_{s0}(1-c)^n, \tag{27}$$

where the exponent n is computed according to

$$\begin{aligned} n &= 4.35R^{-0.03}, & 0.2 < R < 1, \\ n &= 4.45R^{-0.1}, & 1 < R < 500, \\ n &= 2.39, & R > 500, \end{aligned} \tag{28}$$

and where $R = w_{s0}d/\nu$; see Fredsøe and Deigaard (1992, p. 200). When available the base settling velocity w_{s0} for a given case is based on reported values. Otherwise, it is calculated empirically based on the median grain diameter (and other properties), as described in Appendix B.

4. Numerical solutions and implementation

The model described above is implemented within the popular Matlab environment. All y-derivatives are computed using standard finite difference approximations. Results throughout will make use of logarithmically stretched grids consisting of 100 vertical grid points, which has been found to be sufficient to provide converged results. For the time integration of the governing equations Matlab's ode15s function is employed, which consists of a variable-order and variable-time-step integrator designed for solving stiff systems.

Simulations will be illustrated on both hydraulically smooth and rough beds. In hydraulically smooth conditions, the near wall grid spacing Δy is set such that $\Delta y^+ = \Delta y U_f/\nu \le 1$ at all times, enabling resolution of the viscous sublayer. Alternatively, in hydraulically rough conditions the near wall spacing is set such that $\Delta y/k_N \le 0.01$, in accordance with the criterion suggested by Fuhrman et al. (2010).

The model is programmed modularly, such that *e.g.* all single-underlined or double-underlined terms in the governing equations may be included or excluded, respectively, with single switches. Similarly, high-concentration effects (turbulence suppression and hindered settling) may be switched on or off, as desired. The terms or phenomena included in various simulations will be made clear on a case-by-case basis in what follows.

It can be noted that the present model builds on several recent approaches for the RANS-based simulation of turbulent wave boundary layers utilizing two-equation turbulence closures. For example, Holmedal and Myrhaug (2009) have incorporated streaming effects in a similar way within a $k - \epsilon$-based approach, but did not consider high concentration effects (hindered settling and turbulence damping). Alternatively, Ruessink et al. (2009) and Hassan and Ribberink (2010) have been the first to consider such high-concentration effects coupled with non-sinusoidal wave shape effects, though their models did not incorporate convective terms and hence are not able to include additional streaming (and related) effects. The present model is in principle capable of including all of these effects simultaneously, while also including effects of a local bed slope, if desired. Hence, the present approach is proposed as a useful means for studying numerous local effects believed to be important within intra-wave cross-shore sediment transport in a unified fashion.

Solving RANS-based equations in Matlab, the model described in the present paper has been dubbed the "MatRANS" model by the authors. By using the popular Matlab environment, it is hoped that it might make turbulence and/or sediment transport modeling of certain boundary layer and sediment transport processes readily accessible to researchers, engineers and students alike. Therefore, we are happy to make the code (composed primarily of two Matlab M-files), complete with numerous examples set up, available to others upon request to the corresponding author.

5. Hydrodynamic simulations

We will now illustrate various applications of the numerical model described above. The present section will focus on pure hydrodynamic cases, whereas cases involving sediment transport will be the focus of Section 6. As such, throughout the present section, the sediment transport model is switched off, with the remaining model based entirely on the RANS equations and turbulence model, as described in Section 2. It can be additionally noted that, as there is no sediment in the model, the turbulence suppression (double-underlined) terms in Eqs. (3) and (4) are likewise switched off. To illustrate the flexibility of the model, both hydraulically smooth and rough conditions will be considered in what follows. For simulations of flow over smooth beds, the model roughness k_N is kept small, such that $k_N^+ = k_N U_f/\nu \le 1$ at all times. Alternatively, hydraulically rough conditions are set up such that k_N^+ exceeds 100 at some point during the oscillatory flow cycle, ensuring that any Reynolds number dependence is essentially eliminated.

5.1. Oscillatory turbulent wave boundary layers

As a first means of validating the model, oscillatory wave boundary layers beneath sinusoidal free-stream flows will be considered. Hence, the flow is driven by pressure gradients based on the free stream acceleration (Eq. (17)), with $U_{2m} = 0$. For validation purposes, we will compare model results for the wave friction factor f_w, defined according to

$$\frac{\tau_{b,max}}{\rho} = \frac{1}{2}f_w U_{1m}^2 \tag{29}$$

where $\tau_{b,max}$ is the maximum bed shear stress occurring during the model period. This serves as a simple means of validating the model bed shear stresses, the primary driving factor on which sediment transport predictions are based. Comparisons will be made with measurements from oscillating tunnel facilities, hence all single-underlined (streaming) terms are switched off. Comparison with experimental measurements on both smooth and rough beds will be made, for completeness.

Comparisons for hydraulically smooth cases are summarized in Fig. 3, which includes experimental results from Kamphuis (1975), Hino et al. (1983), Sleath (1987), Sumer et al. (1993), and Jensen et al. (1989). Computed results are shown for Reynolds number $Re = aU_{1m}/\nu > 5 \times 10^5$ *i.e.*

after the transition from laminar to fully-turbulent conditions is complete. The model results are seen to fall well within the scatter of the experimental measurements over this range, hence confirming accurate calculation of bed shear stresses in hydraulically smooth conditions. The model results follow closely the empirical relation

$$f_w = 0.04 Re^{-0.16}, \tag{30}$$

which is very similar to equation (2.55) of Fredsøe and Deigaard (1992) (with their coefficient 0.035 replaced by 0.04 in the above).

For hydraulically rough conditions it is well known that f_w does not depend on Re, but rather depends on the non-dimensional roughness a/k_N. Similar to before, the computed results are summarized in the friction factor diagram depicted in Fig. 4, which includes experimental data of Bagnold (1946), Kamphuis (1975), Jonsson and Carlsen (1976), Sleath (1987), Sumer et al. (1987), Jensen et al. (1989), and Dixen et al. (2008). As shown, these data match reasonably the empirical expression

$$f_w = \exp\left(5.5\left(\frac{a}{k_N}\right)^{-0.16} - 6.7\right). \tag{31}$$

This expression has been modified from equation (1.2.23) of Nielsen (1992), to provide a better match with the recent data of Dixen et al. (2008) for small a/k_N values. As seen in Fig. 4, the model results compare reasonably with the experimental values for $a/k_N \geq 20$, and are especially good for $a/k_N \geq 100$. For lower values of a/k_N the roughness length scale k_N becomes appreciable relative to the length scales of the flow, characterized by the amplitude of the free stream orbital motion a. In such circumstances, the "lumped" treatment of the bottom roughness inherent within RANS-based approaches becomes inaccurate, resulting in under-predicted friction coefficients (and therefore bed shear stresses) compared to the experimental measurements.

This comparison serves as a first validation of the model for simulating turbulent wave boundary layers. As demonstrated by the friction factor diagrams, the model is capable of accurately predicting bed shear stresses for a wide range of hydraulically smooth and rough conditions.

5.2. Turbulent wave boundary layer streaming

To test the streaming capabilities of the model, we will again consider sinusoidally driven free-stream flows, but now with all single-underlined terms switched on. As before noted, these will include effects of the convective terms, which are known to be responsible for boundary layer streaming beneath progressive wave motions, as first explained for the laminar case by Longuet-Higgins (1953).

Results for the period-averaged velocity profiles after long-time simulations are shown for smooth-turbulent cases in Fig. 5 and for

rough-turbulent cases in Fig. 6. The results can be characterized by the predicted streaming velocity u_S, defined as the period-averaged horizontal Eulerian velocity above the boundary layer. The present results suggest that the streaming velocity u_S beneath progressive sinusoidal waves can, rather generally, be expressed as

$$\frac{u_s C}{U_{1m}^2} = \Psi, \tag{32}$$

where the constant takes a value $\Psi \approx 0.37$ in smooth-turbulent conditions, and a slightly lesser $\Psi \approx 0.34$ in rough-turbulent conditions. As validation of these results, it can be noted that the latter (rough-turbulent) value is in excellent agreement with the (rather limited) range $\Psi = 0.3375 - 0.345$ found recently by Holmedal and Myrhaug (2009), based on similar RANS wave boundary layer simulations coupled with $k - \epsilon$ turbulence closure. Moreover, the present results also support their contention that in rough-turbulent conditions the non-dimensional streaming velocity Ψ is practically independent of the non-dimensional roughness a/k_N. It can finally be mentioned that the Ψ coefficients above for turbulent conditions are all significantly below the well-known value $\Psi = 3/4$ from laminar theory (Longuet-Higgins, 1953). This value has also been confirmed from model simulations in which the turbulence model is switched off.

5.3. Wave boundary layer in converging–diverging tunnel

Having independently validated the hydrodynamic model for wave boundary layer simulations on flat beds above, we will now consider a simulation involving the local effects of a sloping bed on oscillatory flow. Hence, the triple-underlined terms in Eq. (15) will now be made active, thus taking into account the convective acceleration induced by a mildly-sloping converging–diverging tunnel.

For this purpose, we will consider the (smooth-bed) oscillatory flow experiments in a converging–diverging tunnel made by Sumer et al. (1993); see the conceptual sketch provided in Fig. 7. Specifically, we will consider their Test 16, involving a sinusoidal free-stream flow with characteristic velocity $U_{1m} = 1.96$ m/s and period $T = 9.9$ s, with $Re = 6 \times 10^6$. For the purposes of our simulation the model depth is set to match the tunnel half-depth at the measurement position, corresponding to $h_m = h = 0.1$ m. As only the lower half of the domain is directly simulated, computed results will be reflected across the top boundary for presentation purposes. The bed slope is set to $S = -\tan(\beta)$, where $\beta = 1.031°$ corresponds to the half-angle of their sloping tunnel. Note that the negative value for S implies that the convergent direction is in the negative x direction i.e. leftward (see again Fig. 7). It is finally noted
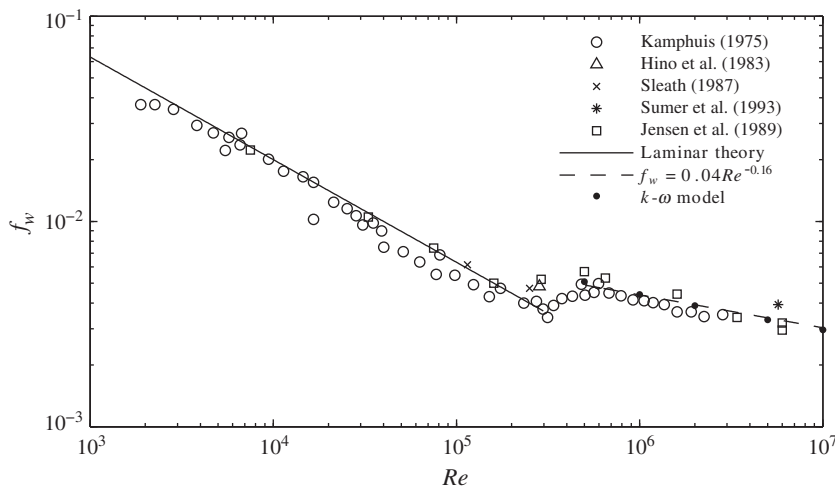

Fig. 3. Comparison of computed and experimentally measured wave friction factors on hydraulically smooth beds.
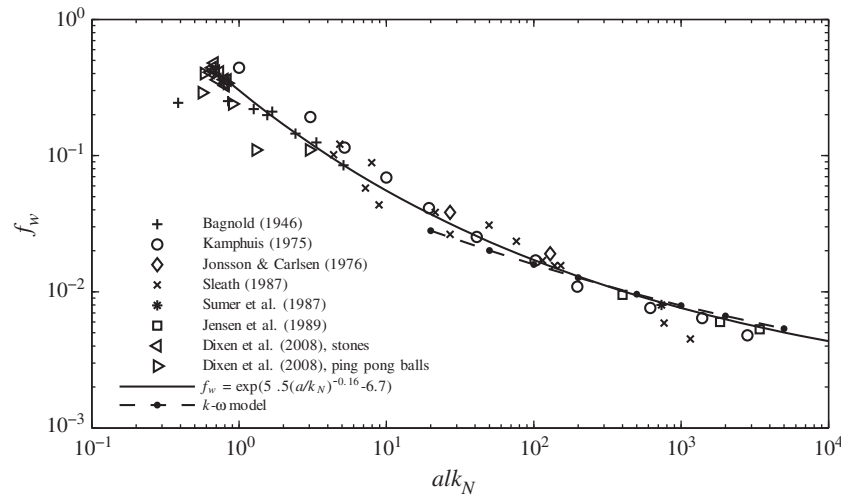
Fig. 4. Comparison of computed and experimentally measured wave friction factors on hydraulically rough beds.

that a constant body force $P_x = -0.0515$ m^2/s has been added to Eq. (15) for the present simulation. This is necessary to ensure a zero net flux of water over the modeled column.

As explained by Sumer et al. (1993), the converging–diverging nature of the present flow environment results in differences in the velocity profiles when averaged over the positive and negative half-cycles. Essentially, the convergent–divergent nature of the tunnel (intended to mimic bed slope effects on the wave boundary layer) will result in increasing pressure in the divergent direction, which will in turn drive a period-averaged near-bed flow in the convergent direction. This is balanced by a return flow higher up in the column, resulting in a circulation pattern depicted in Fig. 7. Model results for the period-averaged velocity profile are depicted in Fig. 8, which compare reasonably with the shown experimental measurements for this case from Sumer et al. (1993).

Note that similar results as shown in Fig. 8 can be seen in Fig. 9b of Fuhrman et al. (2009a), who simulated the oscillatory flow in a converging–diverging tunnel directly in two-dimensions. Hence, the present results demonstrate how such converging–diverging effects may be incorporated directly within a one-dimensional-vertical modeling approach. This is potentially important, as these effects

can give a meaningful contribution to net cross-shore sediment transport rates, as discussed e.g. by Fuhrman et al. (2009b).

6. Sediment transport modeling

The present section will now demonstrate model applications involving sediment transport beneath a variety of wave shapes. In the following, comparison will be made with experimental results on flat beds, hence $S = 0$ throughout. For simulation of oscillatory tunnel conditions, all streaming effects are switched off. Unless otherwise mentioned, all other terms are active in what follows.

6.1. Sediment transport beneath skewed waves

We will begin sediment transport applications by comparing against experimental measurements of O'Donoghue and Wright (2004b), who performed detailed tunnel measurements of sand flux within oscillatory sheet flow conditions. As the present model is restricted to a single grain size, attention will be limited to their cases involving well-sorted sand mixtures, with three median grain diameters $d = 0.15$, 0.28, and 0.51 mm, coupled with two different wave
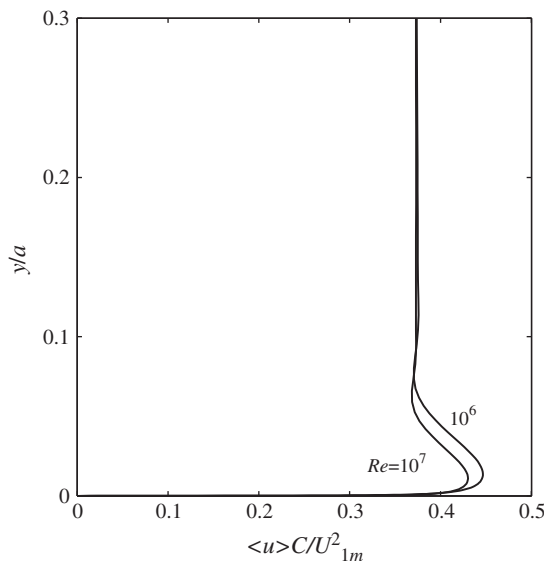

Fig. 5. Computed period-averaged velocity profiles for smooth-turbulent wave boundary layers.
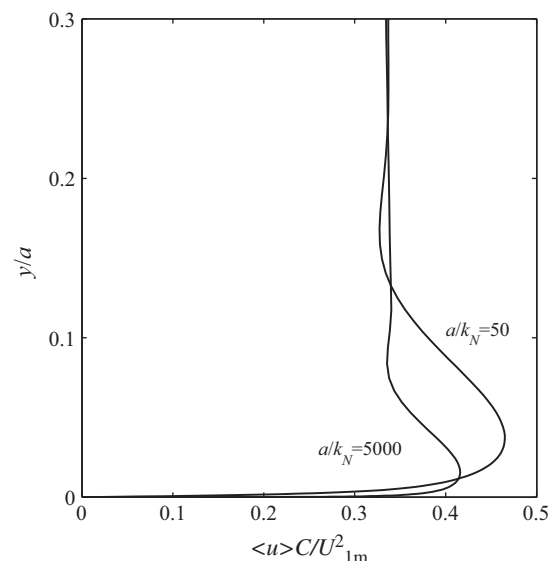

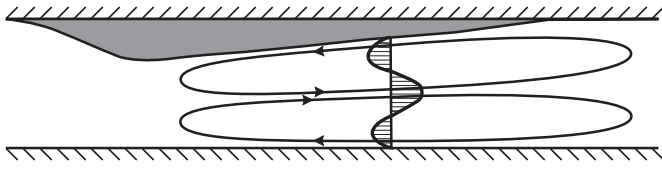**Fig. 6.** Computed period-averaged velocity profiles for rough-turbulent wave boundary layers.

Fig. 7. Conceptual sketch of the recirculating flow system induced by the convergent-divergent geometry of Sumer et al. (1993).

Fig. 9. Free stream velocity signal from O'Donoghue and Wright (2004b).

periods $T = 5$ s and $T = 7.5$ s (*i.e.* six total cases). Their experiments consisted of free stream velocities of the form (16), with velocity magnitudes corresponding to $U_{1m} = 1.21$ m/s and $U_{2m} = 0.31$ m/s, the shape of which is provided in Fig. 9. Hence, these values are utilized within Eq. (17) to drive the modeled flow conditions. The model depth is set to $h_m = 0.25$ m, corresponding to half of the distance from the undisturbed sand bottom to the roof of the experimental tunnel. The experiments on the sand beds were typically carried out over 25 flow cycles. Hence, for comparison all computed results presented will be taken from the 12th cycle *i.e.* corresponding approximately to the middle of the experimental duration. This ensures that the boundary layer within the model domain will be at a similar stage of development as in the experiments. It can be noted that, beyond the first few cycles, the predicted net transport rates vary little (of the order 10%) over the course of the experimental duration, hence the precise cycle considered is of little significance, and is not paramount to any conclusions made herein. Such small variations over the simulated duration are due *e.g.* to the development of a negative drift within the boundary layer, due to asymmetric turbulence levels during peak and trough half-cycles, which is similarly present in the experimental conditions (see Fig. 6a and b of O'Donoghue and Wright, 2004b).

While such comparisons with RANS-based models are typically limited to period-averaged sediment flux profiles (*e.g.* Hassan and Ribberink, 2010), we will here begin by making comparison of instantaneous model predictions directly with measured phase-averaged sediment flux profiles during oscillatory sheet flow conditions. This is intended to provide a sense of how adequately such a RANS-based model can describe the sign, magnitude, and vertical extent of the sediment flux during oscillatory sheet flow conditions. Moreover, to elucidate the influence of high-concentration effects, comparisons will be made using (1) the full version of the model and (2) an
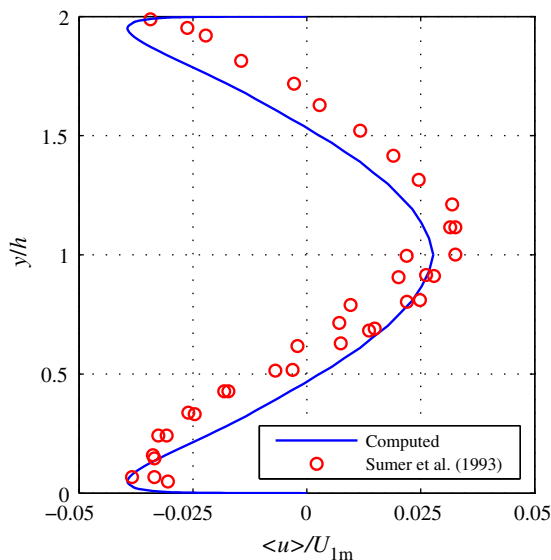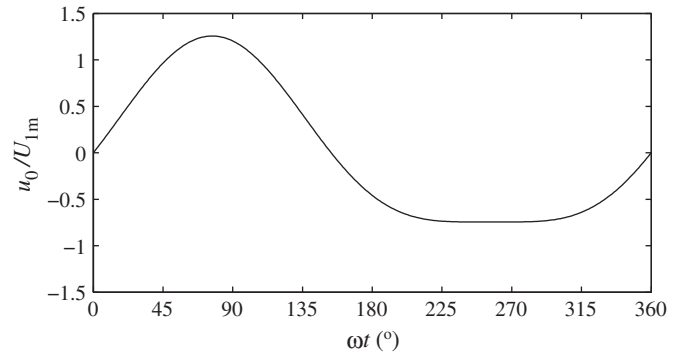
otherwise identical model but with high-concentration effects (*i.e.* hindered settling and turbulence damping) switched off.

O'Donoghue and Wright (2004b) presented detailed (phase-averaged) sediment flux profiles at various phases ωt for two of their cases: FA5010 (fine sand $d = 0.15$ mm and $T = 5$ s), as well as MA5010 (medium sand $d = 0.28$ mm and $T = 5$ s). These cases will serve as the basis for our intra-wave comparison. Results for the sediment flux profiles for the fine sand case FA5010 are first presented in Fig. 10. Obviously, the present model is single-phase, and can therefore not describe the bed erosion and detailed physics of the sheet-flow layer itself (indeed, modeled sediment flux profiles correspond only to $y > b = 2d$). Nevertheless, the full model results (full lines) for the sediment flux profiles consistently resemble the experimental profiles, both in terms of their magnitude, as well as the vertical extent of the sediment flux. In particular, both the experiments and model results illustrate sediment flux profiles largely confined to a thin region of approximately 0.02 m = 2 cm above the bed. In contrast, when the high-concentration effects are neglected (dashed lines) the sediment flux decays much more slowly with distance from the bed. Indeed, for significant portions of the cycle this "standard" model variant predicts significant sediment flux well above the vertical axis limits depicted in the figure, in direct contradiction of the experimental measurements. The reason for this qualitative difference can be traced largely to the influence of the turbulence damping. When included, this effect significantly reduces turbulence levels within the wave boundary layer, which in turn prohibits the vertical diffusion of suspended sediment far above the bed. This comparison highlights the potential importance of including such high-concentration effects in simulations involving the oscillatory sheet flow of fine sands, even at a qualitative level.

So-called phase lag effects (Dohmen-Janssen et al., 2002) are also apparent in both experimental and full model results presented in Fig. 10, wherein sediment stirred up during the positive half-cycle has insufficient time to settle, and is subsequently transported offshore during the negative half-cycle. This is evidenced by the similarity in sediment flux magnitudes predicted at the time of minimum ($\omega t = 259.2°$) and maximum flow velocity ($\omega t = 75.6°$), even though the maximum offshore flow velocity is well below the maximum onshore velocity (see again Fig. 9). These unsteady effects can alter the very direction of net transport, which is discussed in more detail later.

The results for the modeled instantaneous sediment flux profiles corresponding to the medium sand case (MA5010) are likewise depicted in Fig. 11, as are the phase-averaged results of O'Donoghue and Wright (2004b). For most of the flow cycle, the differences between the two model variants is not nearly as significant as for the fine sand case, as the suspended sediment concentration c remains moderate away from the bed. There are noticeable differences around the time of peak flow velocities (*e.g.* $\omega t = 75.6°$ and $118.8°$), however. In contrast to the results for fine sand, these differences are at more of a quantitative, rather than qualitative, level. Phase-lag effects are not

Fig. 8. Comparison of modeled (full line) and measured (circles) period-averaged velocity profile based on test 16 of Sumer et al. (1993).
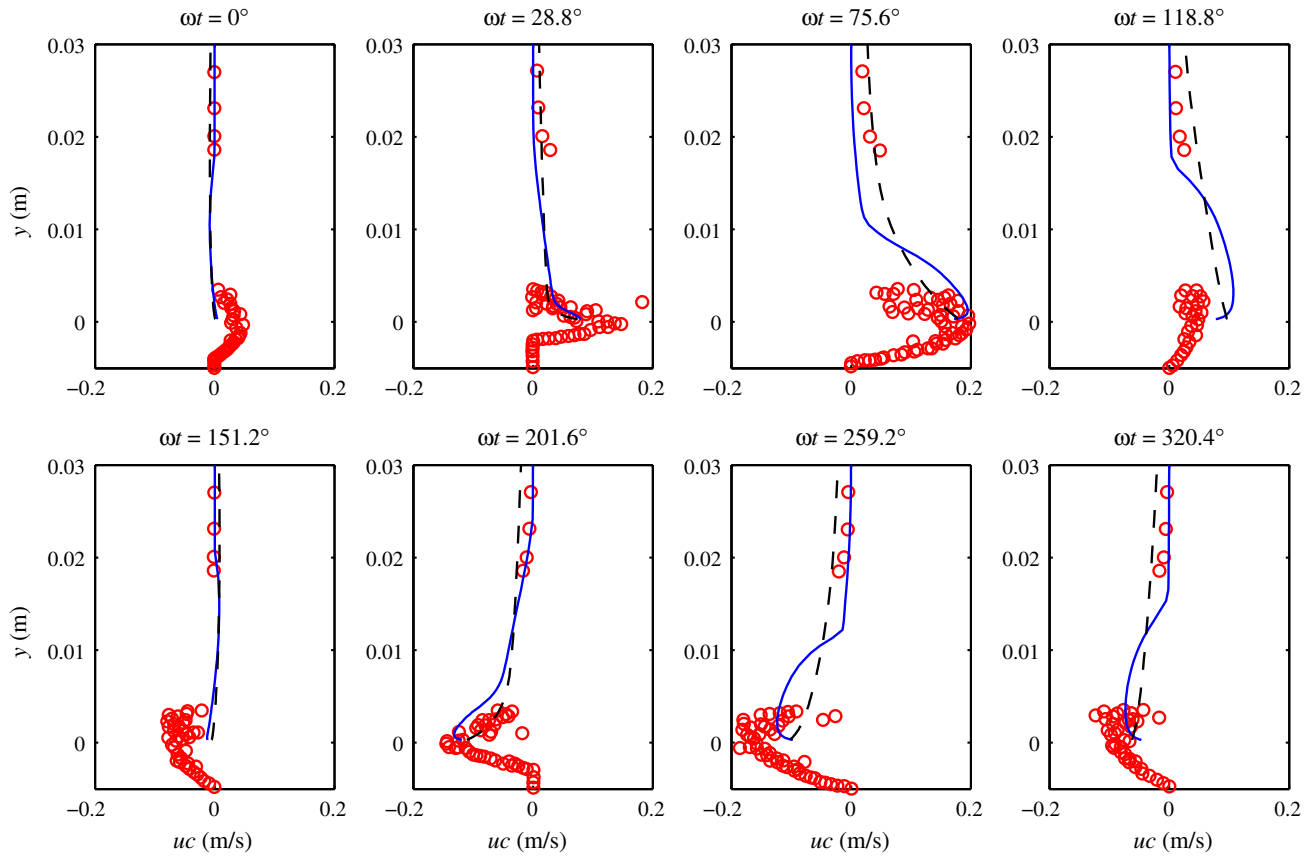
Fig. 10. Comparison of computed (full lines: full model; dashed lines: neglecting high-concentration effects) and measured (circles) sediment flux profiles uc at various phases ωt from experiment FA5010 of O'Donoghue and Wright (2004b).

pronounced in this example. This is evidenced by the significantly lower sediment flux magnitude occurring at the time of maximum offshore velocity ($\omega t = 259.2°$), when compared to the flux occurring during the maximum onshore velocity ($\omega t = 75.6°$).

Computed and measured results for the period-averaged sediment flux profiles for all six of the well-sorted sand cases of O'Donoghue and Wright (2004b) are shown in Fig. 12. Cases presented in this figure are arranged as follows: Top and bottom subplots, respectively, have period $T = 5$ and 7.5 s; left, middle, and right subplots correspond, respectively, to median grain diameters $d = 0.15$, 0.28, and 0.51 mm. As before, full model results are depicted as full lines, whereas the dashed lines depict results predicted by the model with high-concentration effects switched off. It can be noted that Fig. 12a and b depict period-averaged results corresponding to the series of instantaneous flux profiles just presented in Figs. 10 and 11, respectively. Again, there are obvious and inevitable limitations when comparing sediment flux profiles from a fixed-bed model with those from mobile-bed experiments. Nevertheless, and consistent with the previous comparisons, the period-averaged profiles resemble those measured in terms of the direction, magnitude, and total vertical extent of the sediment flux. While we have opted not to do so on the plots to avoid any mis-representation, such resemblances in the profiles can be seen *e.g.* by imagining a 'shifting' of the model results vertically downward.

Among the most notable trends observed from Fig. 12 is the qualitative change from negative sediment flux for fine-sand cases (left-hand subplots) to positive flux for medium- to coarse-grained cases (middle and right-hand subplots). The positive sediment flux for the larger grain sizes is consistent with quasi-steady expectations. Alternatively, the negative sediment flux observed for fine sand cases can be attributed to phase-lag effects alluded to previously (Dohmen-Janssen et al., 2002), wherein sediment stirred up during the positive half-cycle has insufficient time to settle completely, and hence becomes transported in the

opposite direction during the negative half-cycle. The results depicted in Fig. 12a and d suggest that the present unsteady model captures this phenomenon reasonably, with the full model (full lines) yielding flux profiles resembling the nature of those measured. Conversely, and consistent with expectations based on the instantaneous profiles discussed previously for the fine-sand case (Fig. 10), model predictions made without high-concentration effects (dashed lines in Fig. 12a and d) do not at all resemble those measured, either in terms of the magnitude of $\langle uc \rangle$ or its vertical variation and extent. This comparison further supports the necessity of including high-concentration effects for oscillatory sheet-flows involving fine sands.

In addition to the experimental measurements of O'Donoghue and Wright (2004b), Hassan and Ribberink (2005) have likewise conducted a series of oscillating tunnel experiments involving sheet flow beneath skewed free-stream velocity signals of the form (16). Comparison will therefore similarly be made against their pure wave cases (19 in all), having wave periods ranging from $T = 5$ s to 12 s, with uniform sands having median grain diameters ranging from $d = 0.13$ mm to 0.97 mm. For this comparison the model is set up as described previously, with the velocity magnitudes U_{1m} and U_{2m} set in accordance with the reported values for each case. Comparison will be made against their reported period-averaged transport rates for given conditions.

The measured *versus* predicted period-averaged sediment transport rates $q_T = q_B + q_S$ based on the experiments of Hassan and Ribberink (2005) are summarized in Fig. 13. Also included in Fig. 13 are the previously-discussed period-averaged transport rates based on the experiments of O'Donoghue and Wright (2004b). Hence, Fig. 13 summarizes all of the cases considered in the present work involving oscillatory sheet flow beneath skewed free-stream velocity signals. In this figure the full line represents the line of perfect agreement, whereas the dashed lines represent plus or minus a factor of two, often taken as acceptable accuracy when making sediment transport predictions. As
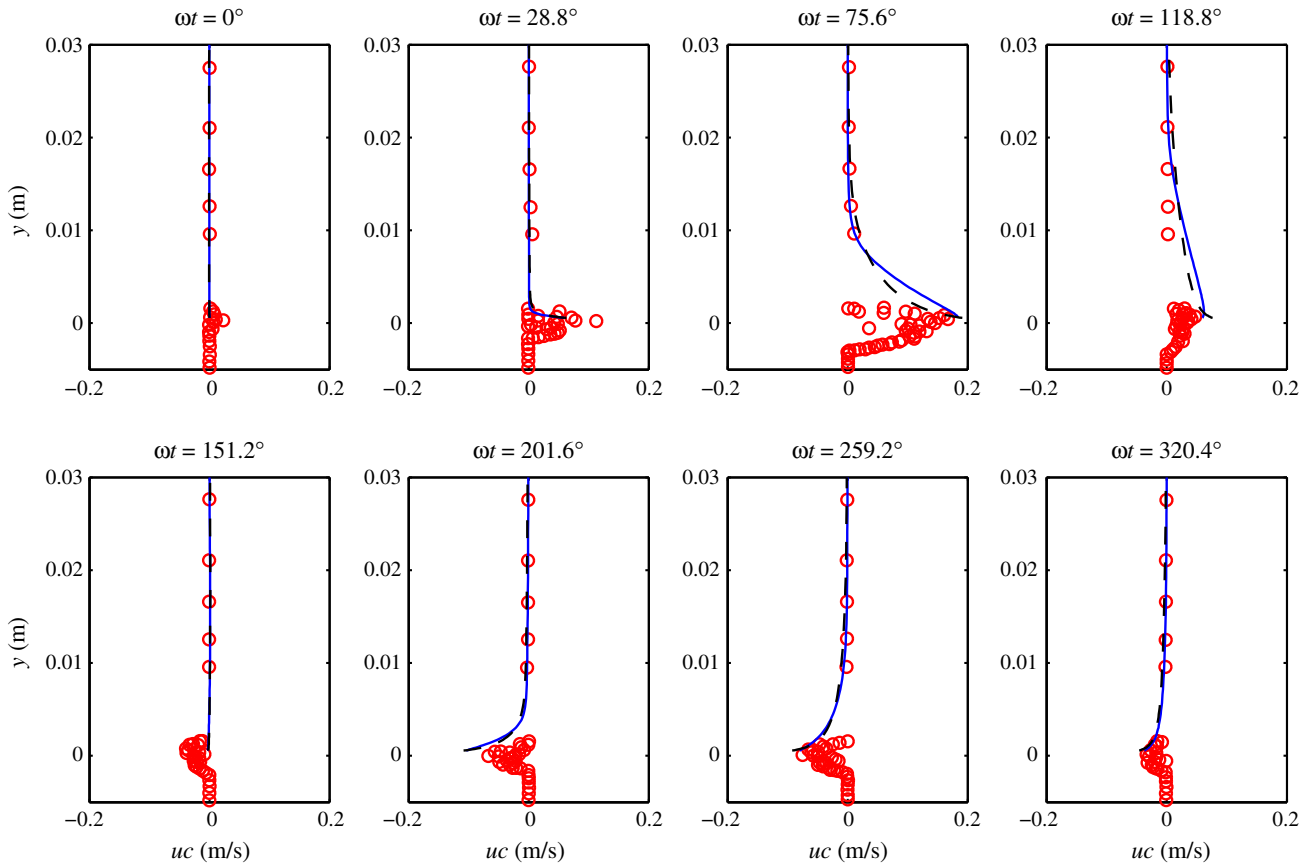
Fig. 11. Comparison of computed (full lines: full model; dashed lines: neglecting high-concentration effects) and measured (circles) sediment flux profiles uc at various phases ωt from experiment MA5010 of O'Donoghue and Wright (2004b).
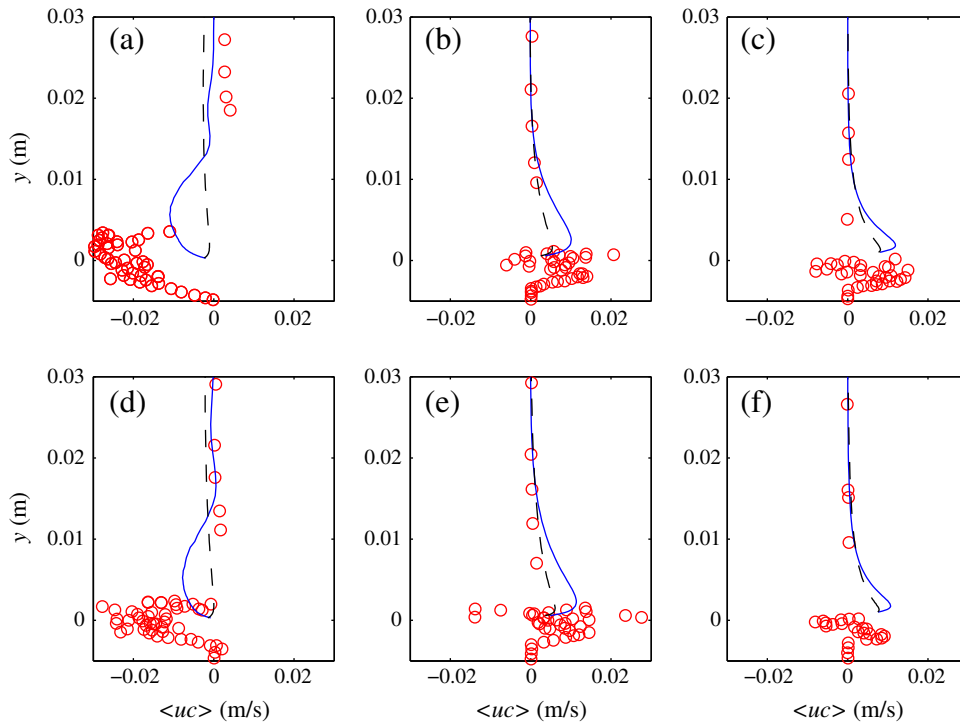

Fig. 12. Comparison of computed (full lines: full model; dashed lines: neglecting high-concentration effects) and measured (circles) period-averaged suspended sediment flux profiles $\langle uc \rangle$ for case (a) FA5010, (b) MA5010, (c) CA5010, (d) FA7515, (e) MA7515, and (f) CA7515 of O'Donoghue and Wright (2004b).
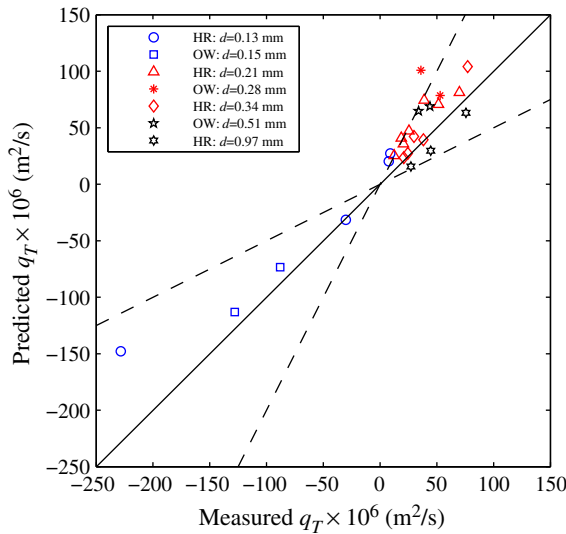
Fig. 13. Summary of measured and predicted period-averaged sediment transport rates q_T for experiments involving skewed free-stream velocity signals. Note that the legend refers to OW: O'Donoghue and Wright (2004b) and HR: Hassan and Ribberink (2005).

Fig. 14. Example of a front-back asymmetric (acceleration skewed) velocity signal from Eq. (18).

can be seen from Fig. 13, two additional cases involving skewed velocity signals and fine sands based on the experimental conditions of Hassan and Ribberink (2005) result in negative transport rates. This is again due to important phase-lag effects, which again seem to be captured reasonably by the present model.

Overall, 100% of the predictions result in the proper sign of net transport, which is not necessarily trivial given the importance of phase lag effects in some cases. Moreover, 20 of the 25 (*i.e.* 80%) predicted transport rates are within a factor two of those measured. Following *e.g.* Ruessink et al. (2009), the present comparison may also be characterized by a prediction skill defined as

$$Sk = 1 - \frac{q_{T,diff}^2}{q_{T,obs}^2}, \tag{33}$$

where $q_{T,diff}$ is the mean-squared difference between the predicted and observed transport rates, whereas $q_{T,obs}$ is the mean-squared observed q_T. Consideration of all 25 cases considered involving sheet flow transport beneath skewed free-stream velocity signals yields an overall prediction skill of $Sk = 0.84$.

We finally mention that, for simplicity, the present results have been presented entirely in terms of the total sediment transport rate q_T. As an indication, however, we mention that for the vast majority of the cases considered the modeled net transport q_T is dominated by the suspended sediment transport contributions q_S, with the bed load contributing not more than 20% of the total (the coarse sand $d = 0.97$ mm cases of Hassan and Ribberink, 2005, being the lone exceptions). This is consistent with the present model strategy of limiting the importance of the quasi-steady bed load predictions during sheet flow conditions, as discussed in Section 3.1. These findings are likewise consistent with those of Hassan and Ribberink (2010), who found similar conclusions regarding the relative importance of quasi-steady bed load predictions within their model. Such results are also consistent with the results of Ruessink et al. (2009), who made accurate sheet-flow sediment transport predictions beneath skewed wave signals without including a separate bed load description.

6.2. Sediment transport beneath asymmetric waves

The previous section considered model comparisons for sheet flow sediment transport rates beneath skewed free-stream velocity
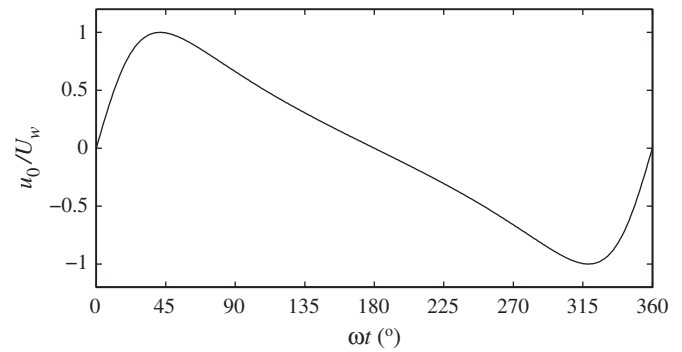
signals *i.e.* those having raised peaks and troughs. However, in reality waves may also be highly asymmetric about their peaks and troughs (*e.g.* sawtooth shaped waves typical of steep slopes and/or within the surf zone). Velocity signals corresponding to such front-back asymmetric waves are commonly referred to as acceleration-skewed in the literature. An example of such an acceleration-skewed velocity signal is depicted in Fig. 14, for clarity.

To investigate the model performance in predicting sediment transport beneath velocities typical of such asymmetric waves, comparison will be made against the recent measurements of van der A et al. (2010), who conducted a series of 35 tests involving sheet flow sediment transport beneath acceleration-skewed velocity signals in an oscillating tunnel. This data set covers a variety of acceleration-skewed velocity signals, with wave periods ranging from $T = 5$ s to 9 s, for median sediment grain diameters of $d = 0.15$, 0.27, and 0.46 mm. Precise flow specifications are detailed on a case-by-case basis within Table 1 of van der A et al. (2010), hence they are not repeated here.

These conditions are simulated as before, but now with the driving pressure gradient based on Eq. (19), with $\phi = 0$ (sawtooth shaped flows). To match the reported velocity signal as closely as possible, the velocity magnitude U_w is set to be the average of the reported peak and trough magnitudes in the experiments, which were typically very close to one another. The shape parameter r is likewise set to yield the precise acceleration skewness coefficient β reported by van der A et al. (2010), based on equation (14) of Abreu et al. (2010). The model depth is set to $h_m = 0.25$ m, again corresponding to half the distance from the top of the sand bed to the tunnel height used in the experiments. Each experiment lasted for 25 flow cycles, hence simulated results will again be taken from the 12th flow cycle *i.e.* approximately in the middle of the experimental duration, as before.

Results for the measured *versus* predicted period-averaged sediment transport rates q_T for all 35 cases are summarized in Fig. 15. As in the previous comparison made using skewed velocity signals, the predicted net transports q_T are dominated by the suspended sediment contribution, with bed load contributions comprising not more than $O(10\%)$. Unlike the previous comparison (Fig. 13), it is seen that all predicted/measured transport rates are now positive. While there is considerable scatter, overall 33 of the 35 predictions (94%) for the period-averaged transport rates fall within a factor two of the measured values, resulting in a prediction skill of $Sk = 0.92$. Generally, the model results for the sediment transport beneath the considered sawtooth-type flows seem comparable in accuracy to the predictions made previously beneath skewed velocity signals (Fig. 13). A systematic trend can, however, be observed in Fig. 15, in that the model predictions gradually shift from under-estimating to over-estimating the transport rates as the sediment size is reduced. Nevertheless, for the range of flow conditions and sediment sizes considered, the overall match with measurements achieved with the present RANS-based approach appears superior to any of the practical sand transport formulations incorporating acceleration skewness considered by van der A et al. (2010).

6.3. Sediment transport beneath progressive waves

The previous two sub-sections have considered the sediment transport beneath both skewed and asymmetric waves under uniform conditions in the horizontal x-direction, as is the situation within oscillatory tunnel environments. In such situations all convective terms can be neglected, as discussed previously. However, in reality progressive waves are not spatially uniform in their propagating direction. The convective terms are thus active, and give rise to period-averaged streaming effects within the boundary layer, as illustrated previously $e.g.$ in Figs. 5 and 6. Such streaming effects are believed to be an important component within cross-shore sediment transport processes.

To investigate such streaming effects on cross-shore sediment transport, comparison will be made against flume measurements beneath progressive waves conducted by Dohmen-Janssen and Hanes (2002). They (in their Table 2) provide measured net sediment transport rates (for median diameter $d = 0.24$ mm) beneath four different progressive regular waves, all of which will be considered. For simulation of these cases, the pressure gradient is prescribed according to Eq. (19), with $\phi = -\pi/2$ $i.e.$ purely skewed velocity signals, as the measurements were taken on a flat bed section. For each case the period T is set to match the experimental value. Dohmen-Janssen and Hanes (2002) report measured mean u_m, crest u_c, and trough u_t velocity values at a prescribed distance from the bed. Hence, the free-stream velocity magnitude for the simulations U_w is set based on the difference in the reported crest and trough values $i.e.$ $U_w = (u_c - u_t)/2$. Similarly, the nonlinearity parameter r is set such that the maximum and minimum in the analytical velocity signal (Eq. (18)) deviate from the mean by the same amount as in the experiments $i.e.$ such that $u_{max} = u_c - u_m$ and $u_{min} = u_t - u_m$. These settings ensure that the driven velocity signal closely resembles that measured beneath the experimental waves. For completeness and repeatability, the precise settings utilized are indicated in Table 1. For these cases the wave celerity C is computed from the linear dispersion relation, based on the reported water depth above the sand bed $h = 3.5$ m. This yields $C = 5.53$ and 5.69 m/s, for $T = 6.5$ and 9.1 s, respectively.

Simulations are run for 100 wave cycles, matching the longest reported experimental duration (stated to last between 30 and 100 wave cycles). Dohmen-Janssen and Hanes (2002) present their measured net transport rates $versus$ the period-averaged cube of the measured velocity signal $\langle u^3 \rangle$ at a prescribed vertical position. Their experimentally measured values are plotted in the same fashion in Fig. 16. For completeness, net transport measurements based on

Table 1
Summary of values used in simulation of measurements beneath progressive waves by Dohmen-Janssen and Hanes (2002).

Case	T (s)	U_w (m/s)	r
mi	6.5	0.885	0.309
mh	6.5	0.905	0.463
mf	9.1	1.005	0.610
me	9.1	1.045	0.734

both their mass conservation as well as flux profile techniques are included. Also depicted in Fig. 16 are the resulting net transport rates from the numerical model, taken from the flow cycle yielding essentially the same value for $\langle u^3 \rangle$ as in the experiments, for consistency. As seen in Fig. 16, the computed values (filled squares) match the measured values (triangles) reasonably, with both supporting a roughly linear relationship between q_T and $\langle u^3 \rangle$. When compared to the values measured via mass conservation, the model results tend to somewhat over-predict the mean transport rate, whereas the computed results are in excellent agreement with (two out of the three) measurements based on the sediment flux profile. In all cases, the computed results are within a factor two of those measured, hence they would seem of similar accuracy as the previous comparisons against measurements made in oscillating tunnels.

Streaming (and related convective) effects can, of course, not be switched off beneath real progressive waves. However, they may easily be either included or excluded within the present idealized numerical environment. Hence, for comparative purposes, simulations for the above four cases have been repeated, maintaining an identical set up and procedure as before, but now with streaming effects ($i.e.$ all single-underlined terms in the governing equations and model forcing) switched off. The resulting net transport rates are likewise shown in Fig. 16 as open squares. As should be expected, the period-averaged net transport rates are reduced without streaming. From the trend lines in Fig. 16 (individually fitted to both sets of computed values), it is seen that the difference in the two sets of predicted transport rates is roughly constant. For case 'mi', having the smallest wave nonlinearity, the streaming amplifies the net transport rate by nearly a factor of two. Alternatively, the percentage increase due to streaming effects is reduced as the wave nonlinearity (and hence $\langle u^3 \rangle$) increases, where net transports induced by the wave shape become more dominant. The roughly constant predicted increase in the transport rate due to streaming effects is consistent
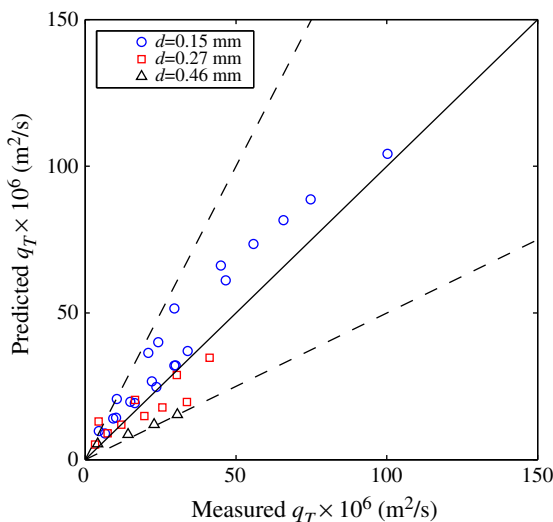
Fig. 15. Summary of predicted net sediment transport for experiments involving acceleration-skewed cases from van der A et al. (2010).
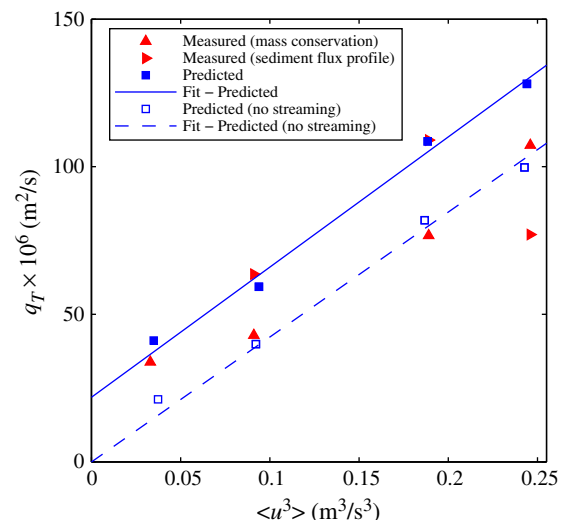
Fig. 16. Comparison of measured and predicted net sediment transport beneath progressive waves, based on experiments of Dohmen-Janssen and Hanes (2002).
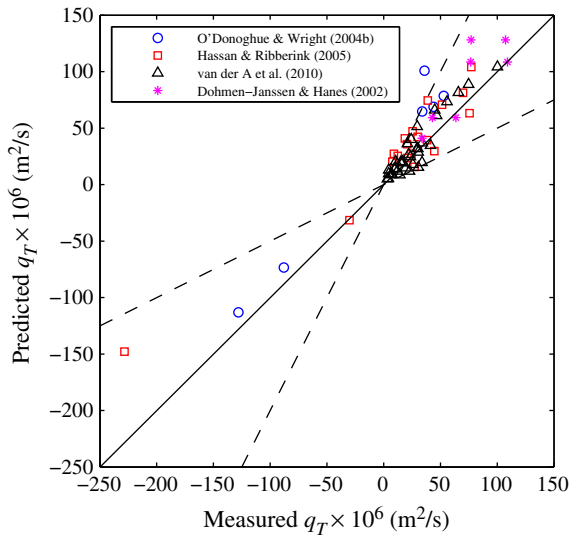
Fig. 17. Comparison of measured and predicted net sediment transport for all cases considered.

with the fact that the ratio U_w/C (a dimensionless measure of streaming importance) varies little (between 0.16 and 0.18) in the present four conditions. This roughly constant value difference is in contrast to the constant factor of approximately 2.5 suggested by the comparison of waves and oscillatory flow made by Dohmen-Janssen and Hanes (2002). Obviously, understanding and quantifying these differences in general still requires further study.

6.4. Summary of sediment transport predictions

To summarize, computed experimental and model results from Figs. 13, 15, and 16 are combined in Fig. 17. Hence, this figure shows all cases, based on (1) velocity-skewed free-stream signals in oscillation tunnels (Hassan and Ribberink, 2005; O'Donoghue and Wright, 2004b), (2) acceleration-skewed free-stream signals in oscillating tunnels (van der A et al., 2010), and finally (3) results beneath progressive waves (Dohmen-Janssen and Hanes, 2002). There is considerable scatter around the line of perfect agreement, which is typical of such comparisons within the field of sediment transport. Combined, model comparisons against 100% of these cases has yielded the correct sign of net transport. Additionally, 57 of the 64 (89%) predictions made are within a factor two of measurements. Consideration of all the data yields an overall prediction skill of $Sk = 0.84$. Hence, the present model seems capable of simulating sediment transport beneath a variety of wave shapes and sediment grains sizes.

The resulting model seems to be comparably accurate e.g. to recent RANS-based approaches of Ruessink et al. (2009) and Hassan and Ribberink (2010), based on $k - \epsilon$ closure. In addition to the high-concentration effects (hindered settling and turbulence damping) included within these earlier studies, the present model is also capable of including important effects associated with boundary layer streaming, as well as converging–diverging effects associated with sloping beds. It is likewise not limited to strict hydraulically rough conditions. Hence, the present model offers a more complete and general description of many locally-important factors potentially affecting cross-shore wave boundary layer and sediment transport processes in the coastal environment.

6.5. Streaming and fine-grain sediment transport beneath skewed waves

As final applications of the present model, we will investigate the potential for streaming (and related convective) effects beneath progressive waves to reverse the direction of fine-grained sediment transport

beneath skewed waves. In particular, from Fig. 13, the previous comparisons against oscillating tunnel set-ups based on the experimental conditions of O'Donoghue and Wright (2004b) and Hassan and Ribberink (2005) included four distinct cases resulting in negative net transport rates due to phase-lag effects; period-averaged sediment flux profiles for two of these are again illustrated in Fig. 12a and d. Hence, for comparative purposes, we will now repeat the simulation of these four cases, but with streaming effects (i.e. all single-underlined terms) switched on. For consistency, for each of these cases we fix the wave celerity C such that $U_{1m}/C = 0.15$. This is a reasonably conservative value for skewed wave conditions in the nearshore environment; indeed, strict application of Stokes second-order theory based on the experimental velocity signals would suggest U_{1m}/C values at least this large, if not larger.

As an example, the results from two simulations based on case FA7515 of O'Donoghue and Wright (2004b) are provided in Fig. 18. This figure shows computed period-averaged vertical profiles for u, c, and their product uc. As seen in Fig. 18c, the inclusion of streaming effects is indeed sufficient to reverse the direction of net transport from the negative (offshore) to the positive (onshore) direction. However, the explanation of this qualitative change cannot be explained by mere examination of the period-averaged velocity profiles (Fig. 18a). While these are expectedly increased due to streaming effects associated with the convective terms in Eq. (1), the period-averaged horizontal velocities remain negative within the boundary layer in both cases, due to the dominance of turbulence-induced streaming effects associated with the skewed velocity signal. It is noteworthy that the streaming effects do not modify the computed period-averaged concentration profile (Fig. 18b) significantly.

To gain further insight, we therefore decompose the period-averaged local flux of suspended sediment according to

$$\langle uc \rangle = \langle u \rangle \langle c \rangle + \langle \tilde{u} \tilde{c} \rangle, \qquad (34)$$

where $u = \langle u \rangle + \tilde{u}$ and $c = \langle c \rangle + \tilde{c}$, i.e. the individual variables are decomposed into their average and fluctuating parts. These individual contributions to $\langle uc \rangle$ are shown in Fig. 19. Fig. 19a is merely the product of Fig. 18a and b, and is hence negative. Alternatively, the period-averaged product of the fluctuations $\langle \tilde{u} \tilde{c} \rangle$ is significantly increased to the onshore (positive) direction when streaming effects are included. This can be largely traced back to the convective terms within Eq. (24), from which e.g. the vertical velocities affect the suspension and settling of suspended sediment asymmetrically during the positive and negative half-cycles of the flow. These terms tend to increase (decrease) the amount of sediment in concentration during the positive (negative) half-cycles. Hence, these effects can be expected to be especially important when the ratio v/w_s is appreciable within the wave boundary layer.

Results from the other three cases have been found to be qualitatively similar to the example just discussed. These results are summarized in Fig. 20, which shows the predicted net transport rates for all four cases with and without streaming effects. Also shown are the original measured values from the oscillating tunnel facility, for reference and completeness. As this figure illustrates, for each of the four cases considered, the inclusion of streaming effects is sufficient to promote net onshore-directed sediment transport. This is in stark contrast to the offshore transport rates predicted for these conditions based on either the oscillatory tunnel experiments or model predictions made with streaming effects excluded. Hence, these results suggest that effects associated with convective terms cannot necessarily be neglected when making cross-shore sediment transport predictions. This is especially the case for situations involving fine sands beneath skewed waves, where such neglect can alter the very sign of predicted net sediment transport.

The present finding that streaming (and related convective) effects can reverse the direction of predicted fine-grain sediment transport
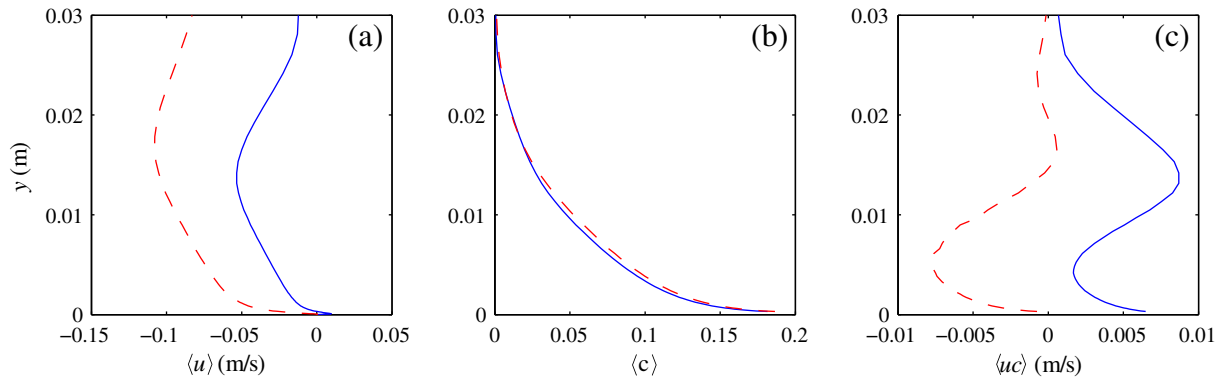
Fig. 18. Computed period-averaged (a) horizontal velocity, (b) sediment concentration, and (c) suspended sediment flux profiles based on case FA7515 of O'Donoghue and Wright (2004b). Results are shown for simulations with streaming effects included (full lines) and excluded (dashed lines).

beneath skewed wave signals (relative to that predicted by oscillating tunnel environments) is supported by recent experimental observations (Schretlen et al., 2011) beneath progressive waves. It is likewise consistent with the very recent work of Blondeaux et al. (2012), who similarly conducted RANS-based simulations comparing sediment transport rate predictions for oscillating tunnel and progressive wave conditions. It should be stressed, however, that their developed model does not include high-concentration effects of hindered settling or turbulence damping. Given the demonstrated significance of these effects in sheet flow conditions involving fine sands (see again *e.g.* Fig. 12a and d), *i.e.* the precise conditions of interest for this phenomenon, it is anticipated that the present model might give a more complete and detailed description of the transport-reversal phenomenon in question.

7. Conclusions

A numerical one-dimensional (vertical) finite-difference model solving Reynolds-averaged Navier–Stokes (RANS) equations, coupled with two-equation $k-\omega$ turbulence closure (Wilcox, 2006) is presented. The hydrodynamic model is coupled with a bed load sediment transport description, in addition to a turbulent-diffusion model for the simulation of suspended sediment concentrations and fluxes. The developed model additionally incorporates (1) hindered suspended sediment settling velocities at high concentrations, (2) turbulence damping due to density gradients in the sand–water mixtures, (3) boundary layer streaming effects stemming from convective terms, as well as (4) converging–diverging effects due *e.g.* to sloping beds. The model is solved within the popular Matlab environment, and is hence potentially attractive for both research and educational purposes.

While the model can, in principal, be applied for simple steady and unsteady flows, the present work has focused on the simulation of turbulent wave boundary layer processes. The basic hydrodynamic model has first been validated by considering sinusoidal free stream flows over both hydraulically smooth and rough beds. Systematic comparison with oscillating tunnel experiments (in the form of wave friction factor diagrams) in both situations demonstrates good accuracy in the model bed shear stress predictions, a key quantity in making sediment transport rate predictions. Moreover, model predictions for the boundary layer streaming velocities beneath sinusoidal progressive waves have demonstrated an excellent match with previous simulations. Model results support the contention of Holmedal and Myrhaug (2009) that the non-dimensionalized streaming velocity on rough beds is essentially constant, and demonstrates similar findings on smooth beds. Finally, comparison against period-averaged velocity profile measurements made by Sumer et al. (1993) within an oscillating converging–diverging flow demonstrate the adequacy of this feature within the model.

In addition to the basic hydrodynamic validation described above, an extensive number of simulations involving sediment transport beneath a wide variety of wave shapes, periods, and sediment grain sizes in oscillating tunnel conditions have been presented. Nonlinear wave shapes in the coastal environment can range from highly skewed (raised peaks and troughs) to highly front-back asymmetric (*e.g.* sawtooth shapes). As validation for sediment transport rate predictions beneath skewed waves, model results have been compared with oscillating tunnel measurements of O'Donoghue and Wright (2004b) and Hassan and Ribberink (2005), generally demonstrating acceptable accuracy (predictions within a factor of two for the vast majority of cases). Comparisons with the detailed intra-wave sediment flux profiles of O'Donoghue and Wright (2004b) illustrate the ability of the model to
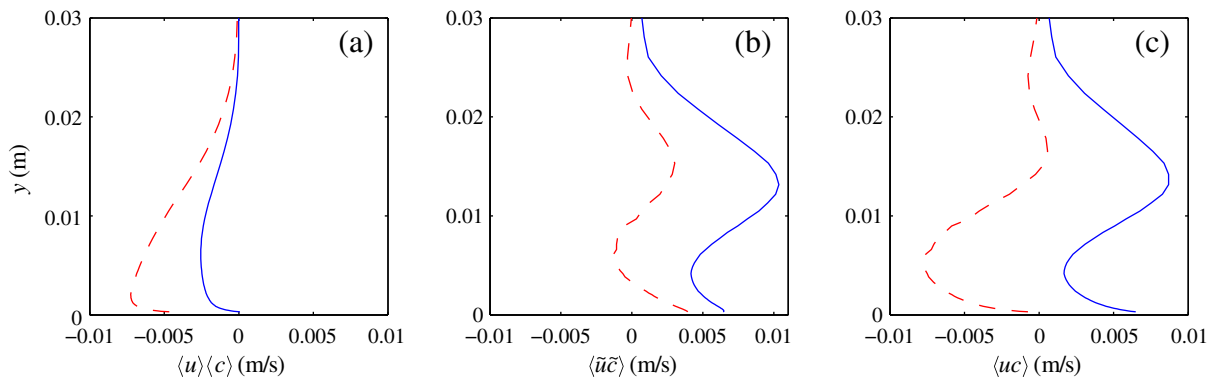

Fig. 19. Computed results for the components of the period-averaged suspended sediment flux according to Eq. (34), based on case FA7515 of O'Donoghue and Wright (2004b). Results are shown for simulations with streaming effects included (full lines) and excluded (dashed lines).
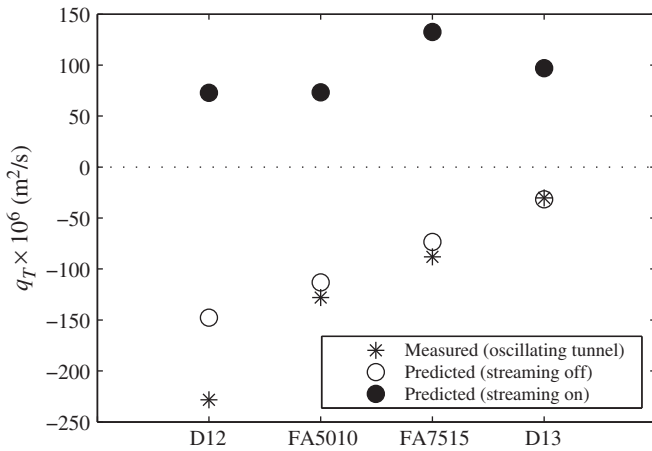
Fig. 20. Summary of selected results involving fine sands beneath skewed velocity signals with streaming effects included and excluded. The x-axis labels correspond to the experimental cases from O'Donoghue and Wright (2004b) and Hassan and Ribberink (2005).

predict reasonably accurate flux magnitudes, as well as the vertical extent of transport, throughout the wave cycle. Comparisons made with high-concentration effects (hindered settling and turbulence damping) switched off, additionally suggest that such a "standard" approach can dramatically over-estimate the vertical extent of suspended fine sands, hence supporting the inclusion of these effects in such circumstances. Applications of the full model demonstrate the ability to faithfully capture unsteady phase-lag effects, which can reverse the direction of net transport in oscillating tunnels from positive (onshore) to negative (offshore) for cases involving fine sands coupled with sufficiently short wave periods. Similar comparisons with the extensive data set of van der A et al. (2010) have likewise demonstrated comparable accuracy in making net transport rate predictions for asymmetric (sawtooth-type) acceleration-skewed signals in oscillating tunnel conditions.

While oscillating tunnel experiments have been the experimental basis for much of our present knowledge of turbulent wave boundary and sediment transport processes, due to their spatial uniformity, they do not incorporate any effects of boundary layer streaming, stemming from convective terms. Therefore, additional simulations (with convective terms included) have been made based on measurement conditions beneath skewed progressive waves made by Dohmen-Janssen and Hanes (2002)) for medium sand grains. Consistent with the measurements, the sediment transport rate predictions in these circumstances are all positive, with magnitudes in reasonable agreement with those measured. To illustrate the relative importance of streaming effects, the simulations have likewise been repeated with convective terms excluded. Comparison of the results suggests that, for the conditions considered, streaming effects can amplify the predicted sediment transport rates by as much as a factor of two. The results likewise suggest that the relative importance of streaming depends strongly on the wave shape, however. For highly skewed waves, the wave shape can be the dominant contributor to the net sediment transport.

Due to phase-lag effects, it is well-known that oscillating tunnel experiments involving skewed waves and fine sands can yield negative (offshore) net sediment transport rates, as discussed above. However, whether this reversal in the sign of transport occurs beneath real progressive waves (i.e. active convective terms) is an open question. To investigate the potential for streaming effects to re-reverse the sign of net transport (back to positive) in these situations, the four conditions resulting in negative transport rates have been repeated, but with streaming effects switched on, to mimic the expected behavior beneath real progressive waves. In each of the four cases, the results indeed suggest, that streaming (and related convective) effects can indeed change the sign of net transport from negative to positive. Hence, simultaneous

inclusion of all relevant convective terms may be necessary in such circumstances, as doing otherwise can alter the very direction of predicted net transport rates. This result adds further insight and support to recent experimental (Schretlen et al., 2011) and numerical (Blondeaux et al., 2012) findings regarding this issue.

The model utilized throughout the present study has been developed within the popular Matlab environment, and hence may be of interest for both research, as well as educational, purposes. Therefore, upon publication of this article, the code (complete with numerous example set ups) will be made available, upon request to the corresponding author.

Appendix A. Converging–diverging pressure gradient terms

In this appendix a brief explanation of the converging–diverging flow contribution to the driving pressure gradient (Eq. (15)) is provided. A converging tunnel (with local depth h at $x = 0$ and slope S) leads to the depth variation

$$h(x) = h - Sx. \tag{A.1}$$

For a particular discharge (per unit width) q, the mean horizontal velocity (here taken as the free stream velocity u_0, assuming small boundary layer thickness) will then vary according to

$$u_0(x) = \frac{q}{h(x)} = \frac{q}{h - Sx} = u_0 + u_0 \frac{Sx}{h} + O\left(\frac{x^2 S^2}{h^2}\right), \tag{A.2}$$

taking $u_0 = u_0(x = 0) = q/h$. Hence, at leading-order, the additional contribution to the convective terms (at $x = 0$) becomes

$$u_0 \frac{\partial u_0}{\partial x} = \frac{S u_0^2}{h}, \tag{A.3}$$

which matches the triple-underlined term in Eq. (15). This approximation should therefore be valid for simulating local converging–diverging flows on mild bottom slopes.

Notice that, as implemented, the prescribed flow depth h may deviate from the actual model depth h_m. This allows inclusion of converging–diverging effects associated with a sloping bed, without necessarily resolving the entire flow depth, which may be convenient within wave boundary layer simulations.

Appendix B. Explicit evaluation of the settling velocity

By considering equilibrium of gravity, buoyancy, and drag forces the settling velocity may be express as

$$w_{s0} = \sqrt{\frac{4(s-1)gd}{3c_D}}. \tag{B.1}$$

From e.g. Fredsøe and Deigaard (1992), the drag coefficient c_D can be expressed as a function of the Reynolds number $R = w_{s0}d/\nu$:

$$c_D = 1.4 + \frac{36}{R}. \tag{B.2}$$

Squaring Eq. (B.1) and inserting the expressions above, after some rearrangement leads to a quadratic polynomial in w_{s0}

$$a w_{s0}^2 + b w_{s0} + c = 0, \tag{B.3}$$

where $a = 4.2$, $b = 108\nu/d$, and $c = -4gd(s-1)$. As we are only interested in positive values for w_{s0}, this leads to the following explicit solution for the settling velocity

$$w_{s0} = \frac{-b + \sqrt{b^2 - 4ac}}{2a}, \tag{B.4}$$

which is valid for $R > 1$.

References

Abreu, T., Silva, P.A., Sancho, F., Temperville, A., 2010. Analytical approximate wave form for asymmetric waves. Coastal Engineering 57, 656–667.

Amoudry, L., Hsu, T.-J., Liu, P.L.-F., 2008. Two-phase model for sand transport in sheet flow regime. Journal of Geophysical Research 113 (C03011/1–15).

Bagnold, R.A., 1946. Motion of waves in shallow water. Interaction between waves and sand bottoms. Proceedings of the Royal Society of London Series A 187, 1–15.

Blondeaux, P., Vittori, G., Bruschi, A., Lalli, F., Pesarino, V., 2012. Steady streaming and sediment transport at the bottom of sea waves. Journal of Fluid Mechanics 697, 115–149.

Brøker, I.H., 1985. Wave generated ripples and resulting sediment transport in waves. Series Paper No. 36, ISVA. Technical University of Denmark.

Davies, A.G., Li, Z., 1997. Modelling sediment transport beneath regular symmetrical and asymmetrical waves above a plane bed. Continental Shelf Research 17, 555–582.

Davies, A.G., Ribberink, J.S., Temperville, A., Zyserman, J.A., 1997. Comparison between sediment transport models and observations made in wave and current flows above plane beds. Coastal Engineering 31, 163–198.

Deigaard, R., Jacobsen, J.B., Fredsøe, J., 1999. Net sediment transport under wave groups and bound long waves. Journal of Geophysical Research 104, 13559–13575.

Dixen, M., Hatipoglu, F., Sumer, B.M., Fredsøe, J., 2008. Wave boundary layer over a stone-covered bed. Coastal Engineering 55, 1–20.

Dohmen-Janssen, C.M., Hanes, D.M., 2002. Sheet flow dynamics under monochromatic nonbreaking waves. Journal of Geophysical Research 107, C03149.

Dohmen-Janssen, C.M., Kroekenstoel, D., Hassan, W., Ribberink, J., 2002. Phase-lags in oscillatory sheet flow: experiments and bed load modelling. Coastal Engineering 46, 61–87.

Einstein, H.A., 1950. The bed-load function for sediment transportation in open channel flows. Tech. Rep. Techn. Bulletin No. 1026. U.S. Dept. of Agriculture.

Engelund, F., Fredsøe, J., 1976. A sediment transport model for straight alluvial channels. Nordic Hydrology 7, 293–306.

Fredsøe, J., Deigaard, R., 1992. Mechanics of Coastal Sediment Transport. World Scientific, Singapore.

Fuhrman, D.R., Fredsøe, J., Sumer, B.M., 2009a. Bed slope effects on turbulent wave boundary layers: 1. Model validation and quantification of rough-turbulent results. Journal of Geophysical Research 114, C03024.

Fuhrman, D.R., Fredsøe, J., Sumer, B.M., 2009b. Bed slope effects on turbulent wave boundary layers: 2. Comparison with skewness, asymmetry, and other effects. Journal of Geophysical Research 114, C03025.

Fuhrman, D.R., Dixen, M., Jacobsen, N.G., 2010. Physically-consistent wall boundary conditions for the k–ω turbulence model. Journal of Hydraulic Research 48, 793–800.

Fuhrman, D.R., Sumer, B.M., Fredsøe, J., 2011. Roughness-induced streaming in turbulent wave boundary layers. Journal of Geophysical Research 116, C10002.

Guizien, K., Dohmen-Janssen, M., Vittori, G., 2003. 1dv bottom boundary layer modeling under combined wave and current: turbulent separation and phase lag effects. Journal of Geophysical Research 108 (C1), 3016.

Hassan, W.N., Ribberink, J.S., 2005. Transport processes of uniform and mixed sands in oscillatory sheet flow. Coastal Engineering 52, 745–770.

Hassan, W.N.M., Ribberink, J.S., 2010. Modelling of sand transport under wave-generated sheet flows with a rans diffusion model. Coastal Engineering 57, 19–29.

Hino, M., Kashiwayanagi, M., Nakayama, A., Hara, T., 1983. Experiments on the turbulence statistics and the structure of a reciprocating oscillatory flow. Journal of Fluid Mechanics 131, 363–400.

Holmedal, L.E., Myrhaug, D., 2006. Boundary layer flow and net sediment transport beneath asymmetrical waves. Continental Shelf Research 26, 252–268.

Holmedal, L.E., Myrhaug, D., 2009. Wave-induced steady streaming, mass transport and net sediment transport in rough turbulent ocean bottom boundary layers. Continental Shelf Research 29, 911–926.

Hsu, T.-J., Liu, P.L.-F., 2004. Toward modeling turbulent suspension of sand in the nearshore. Journal of Geophysical Research 109, C06018.

Jensen, B.L., Sumer, B.M., Fredsøe, J., 1989. Turbulent oscillatory boundary layers at high Reynolds numbers. Journal of Fluid Mechanics 206, 265–297.

Jonsson, I.G., Carlsen, N.A., 1976. Experimental and theoretical investigations in an oscillatory turbulent boundary layer. Journal of Hydraulic Research 14, 45–60.

Justesen, P., 1988. Turbulent wave boundary layers. Series Paper No. 43, ISVA. Technical University of Denmark.

Kamphuis, J.W., 1975. Friction factor under oscillatory waves. Journal of Waterway Port, Coastal, and Ocean Engineering Division ASCE 101 (WW2), 135–144.

Li, Z., Davies, A.G., 2001. Turbulence closure modelling of sediment transport beneath large waves. Continental Shelf Research 21, 243–262.

Longuet-Higgins, M.S., 1953. Mass transport in water waves. Philosophical Transactions of the Royal Society of London Series A 245, 535–581.

Meyer-Peter, E., Müller, R., 1948. Formulas for bed-load transport. Rep. 2nd Meet. Int. Assoc. Hydraul. Struct. Res. Stockholm, pp. 39–64.

Nielsen, P., 1992. Coastal Bottom Boundary Layers and Sediment Transport. World Scientific, Singapore.

Nielsen, P., Callaghan, D.P., 2003. Shear stress and sediment transport calculations for sheet flow under waves. Coastal Engineering 47, 347–354.

O'Donoghue, T., Wright, S., 2004a. Concentrations in oscillatory sheet flow for well sorted and graded sands. Coastal Engineering 50, 117–138.

O'Donoghue, T., Wright, S., 2004b. Flow tunnel measurements of velocities and sand flux in oscillatory sheet flow for well-sorted and graded sands. Coastal Engineering 51, 1163–1184.

Richardson, J.F., Zaki, W.N., 1954. Sedimentation and fluidisation, part 1. Transactions of the Institution of Chemical Engineers 32, 35–53.

Ruessink, B.G., van den Berg, T.J.J., van Rijn, L.C., 2009. Modeling sediment transport beneath skewed asymmetric waves above a plane bed. Journal of Geophysical Research 114, C11021.

Schretlen, J.J.L.M., Ribberink, J.S., O'Donoghue, T., 2011. Boundary layer flow and sand transport under full scale surface waves. In: Smith, J.M., Lynett, P. (Eds.), Proc. 32nd Int. Conf. Coastal Engineering. Shanghai.

Sleath, J.F.A., 1987. Turbulent oscillatory flow over rough beds. Journal of Fluid Mechanics 182, 369–409.

Sumer, B.M., Jensen, B.L., Fredsøe, J., 1987. Turbulence in oscilatory boundary layers. In: Comte-Bellot, C., Mathieu, J. (Eds.), Advances in Turbulence. Springer-Verlag, Berlin, pp. 556–567.

Sumer, B.M., Laursen, T.S., Fredsøe, J., 1993. Wave boundary layer in a convergent tunnel. Coastal Engineering 20, 317–342.

Sumer, B.M., Chua, L.H.C., Cheng, N.-S., Fredsøe, J., 2003. Influence of turbulence on bed load sediment transport. Journal of Hydraulic Engineering ASCE 129, 585–596.

Trowbridge, J., Madsen, O.S., 1984. Turbulent wave boundary layers 2. Second-order theory and mass transport. Journal of Geophysical Research 89, 7999–8007.

van der A, D.A., O'Donoghue, T., Ribberink, J.S., 2010. Measurements of sheet flow transport in acceleration-skewed oscillatory flow and comparison with practical formulations. Coastal Engineering 57, 331–342.

Wilcox, D.C., 2006. Turbulence Modeling in CFD, 3rd edition. DCW Industries, Inc., La Canada, California.

Wilcox, D.C., 2008. Formulation of the k–ω turbulence model revisited. AIAA Journal 46, 2823–2838.

Wong, M., Parker, G., 2006. Reanalysis and correction of bed-load relation of Meyer–Peter and Müller using their own database. Journal of Hydraulic Engineering ASCE 132, 1159–1168.

Zyserman, J.A., Fredsøe, J., 1994. Data analysis of bed concentration of suspended sediment. Journal of Hydraulic Engineering 120, 1021–1042.